Winter Dynamics in an Epishelf Lake: Quantitative Mixing Estimates and Ice Shelf Basal Channel Considerations

J. Bonneau[1], B. E. Laval[1], D. Mueller[2], A. K. Hamilton[3], A. M. Friedrichs[4,5], A. L. Forrest[4,5]

[1]Department of Civil Engineering, University of British Columbia, Vancouver, BC, Canada
[2]Department of Geography and Environmental Studies, Carleton University, Ottawa, ON, Canada
[3]Earth and Atmospheric Sciences, University of Alberta, Edmonton, AB, Canada
[4]Civil and Environmental Engineering, University of California Davis, CA, USA.
[5]Tahoe Environmental Research Center, University of California Davis, CA, USA.

Key Points:

- A one-dimensional model is used to analyse eight years of winter mooring data of the upper water column in an perennially ice-covered fjord.
- Mixing is more pronounced in the isolated freshwater layer (epishelf lake) than in the seawater below.
- Epishelf lake water exits the fjord through a basal channel under the ice shelf. The channel is apparently not evolving rapidly.

Corresponding author: Jrmie Bonneau, `jeremie.bonneau@alumni.ubc.ca`

Abstract

Milne Ice Shelf is located at the mouth of Milne Fiord (82.6°N, 81.0°W), on Ellesmere Island, Nunavut. This floating ice feature is attached to both sides of the fjord. During the melt season, the ice shelf acts as a dam preventing surface runoff from flowing freely to the ocean. This results in a permanent layer of freshwater that "floats" on top of the seawater of the fjord, commonly known as an epishelf lake. The winter data from a mooring installed in Milne Fiord epishelf lake (2011-2019) is analysed in the framework of a one-dimensional model in order to 1) study mixing in the upper water column and 2) infer the characteristics of a basal channel in the ice shelf. The results show that vertical mixing rates are higher in the epishelf lake than in the seawater below. Estimation of the Richardson number using a geostrophic balance approach reveals that enhanced mixing in the epishelf lake is associated with horizontal temperature gradients. Moreover, the analysis suggests that the epishelf lake water reaching the ocean travels through a single basal channel in the ice shelf. The model did not detect significant variation in outflow characteristics over the eight years of study, implying that the area of the basal channel is in ice mass balance.

Plain Language Summary

An ice shelf is a thick floating sheet of ice attached to the land. At the mouth of Milne Fiord, on the northern coast of Ellesmere Island, is Milne Ice Shelf. Milne Ice Shelf is attached to the land on both sides of the fjord and acts like a dam preventing fresh meltwater from the watershed from directly flowing out to the ocean. This creates a layer of freshwater floating on top of the seawater, called an epishelf lake. In this study, we use field observations and a numerical model to conclude that there is more mixing in the epishelf lake than in the seawater below. Moreover, we suggest that most of the water flowing out of the epishelf lake follows a channel under the ice shelf and that this channel has not evolved significantly from 2011 to 2019.

1 Introduction

In the Canadian High Arctic, all major glaciers north of the 74$^{\text{th}}$ parallel are losing mass as a result of atmospheric warming (Mortimer et al., 2018). Climate-related changes are unmistakable on the northern coast of Ellesmere Island where the ice shelf extent has considerably decreased over the last century (Mueller et al., 2017). In this region, where historically there was an ice shelf at the mouth of every fjord (Vincent et al., 2001), the continuous fracture and break up of ice shelves left only one relatively intact in Milne Fiord. portions of the Milne Ice Shelf are attached to land on both sides of the fjord. Therefore, it acts like a dam, preventing freshwater from surface runoff from dispersing freely into the ocean. This perennial layer of freshwater overlying Arctic seawater landward of the ice shelf is referred to as an epishelf lake. Since Milne Ice Shelf (MIS) is the only ice shelf in Canada that had not broken up, Milne Fiord epishelf lake (MEL) is the last epishelf lake along its coast. Several other epishelf lakes can be found in Antarctica (Laybourn-Parry & Wadham, 2014; Gibson & Andersen, 2002) and one in Greenland (Bennike & Weidick, 2001). In late July 2020, ∼43% of MIS calved along its seaward front.

The dynamics of the Milne epishelf lake and Milne Ice Shelf are closely linked. It is thought that the epishelf lake outflows through a basal channel under the ice shelf. Therefore, it is hypothesized that the morphology of the channel controls the thickness of the epishelf lake (Hamilton et al., 2017). The basal channel under Milne Ice Shelf is analogous to those found beneath Petermann Glacier in Greenland (Rignot & Steffen, 2008; Washam et al., 2019) or Pine Island Glacier Ice Shelf (Stanton et al., 2013; Dutrieux et al., 2013) in Antarctica. These basal channels have attracted attention in recent years as meltwater concentrates in these features (Millgate et al., 2013; Gladish et al., 2012)

and increases local melt rates (Stanton et al., 2013; Dutrieux et al., 2013; Alley et al., 2016). It is generally thought that the localized strong melting within channels leads to faster breakup as a result of weakening of the overall structure (Dow et al., 2018; Gourmelen et al., 2017; Rignot & Steffen, 2008). However, numerical modeling has shown that these channels could potentially reduce the overall melting of ice shelf, resulting in a stabilization effect (Gladish et al., 2012).

From an oceanographic perspective, the physical structure of the upper water column in Milne Fiord is well known during summer (Hamilton et al., 2017), but less so during winter. Because the fjord is perennially ice-covered, no wind-induced circulation or mixing occurs. Moreover, the tidal amplitudes are very small ($\sim$10 cm). However, other mechanisms can modify the water column in ice-covered fjords. Sciascia et al. (2013) found that even during the winter, meltwater plumes influenced the circulation in Sermilik Fjord, Greenland. Also in Sermilik, R. H. Jackson et al. (2014) and Straneo et al. (2010) showed that water properties changed in response to along-shore wind episodes creating downwelling events. The Earth's rotation can also alter the currents in a fjord when it is sufficiently wide (i.e. larger than the Rossby radius) (Straneo & Cenedese, 2015; R. H. Jackson et al., 2018), changing the circulation from a two dimensional to a three dimensional pattern.

Furthermore, due to the presence of the ice shelf, the upper water column in Milne Fiord has similarities with ice-covered lakes, where the influence of the Earth's rotation on the circulation pattern has also been reported (e.g. Bengtsson, 1996; Rizk et al., 2014; Huttula et al., 2010; Forrest et al., 2013; Steel et al., 2015). In some cases, heat fluxes at the boundaries combine with Coriolis force to generate circulation features in geostrophic or cyclogeostrophic balance. These boundary heat fluxes can be the result of sediment (Rizk et al., 2014), inflows and solar heating of moat water (Kirillin et al., 2015) or melting of ice along an ice wall (Steel et al., 2015).

Since there is a strong interconnection between the ice shelf, the epishelf lake and the glacier, quantitative information about circulation and mixing processes is important to better understand the outflow in the channel and the amount of surface runoff. Furthermore, this information would also improve insights on the fate of the ice structures in the fjord (e.g. ice shelf, glacier and lake ice). Finally, in addition to other epishelf lakes in Antarctica, physical processes in MEL can be similar to those in ice-covered lakes, where external forcing is limited, especially when snow cover significantly reduces solar radiation reaching the water. Since it is perennially ice-covered, Milne epishelf lake studies also provide an understanding of ice-covered lake processes.

This study has two main objectives. The first is to quantify vertical mixing occurring in the epishelf lake and associate it with a forcing mechanisms. The second is to confirm that the basal channel is the main outflow path for the epishelf lake and to infer the evolution of its morphology. In order to do this, a one-dimensional model was calibrated with the mooring data (July 2011 to July 2019) to estimate the mixing in the top of the water column and the discharge through the channel in winter.

2 Geophysical Setting and Study Area Background

2.1 Milne Fiord

Figure 1 is a satellite image of Milne Fiord showing the downstream part of Milne Glacier (MG), the glacier tongue (MGT), the epishelf lake (MEL) and the ice shelf (MIS). The main part of MEL is between MIS and MGT, although there is an arm on each side of MGT. Milne Fiord is 40 km long from the glacier grounding line to the outer edge of the ice shelf (prior to the 2020 calving event). Its width is 6 km from the glacier grounding line to the epishelf lake and then becomes wider downfjord. The bathymetry of the fjord, inferred from CTD casts and depth soundings (Hamilton et al., 2017) exhibits a U-shape profile with a maximum depth of 436 m. A 220 m deep sill is inferred to exist just downfjord of the epishelf lake. The maximum fjord depth below the epishelf lake

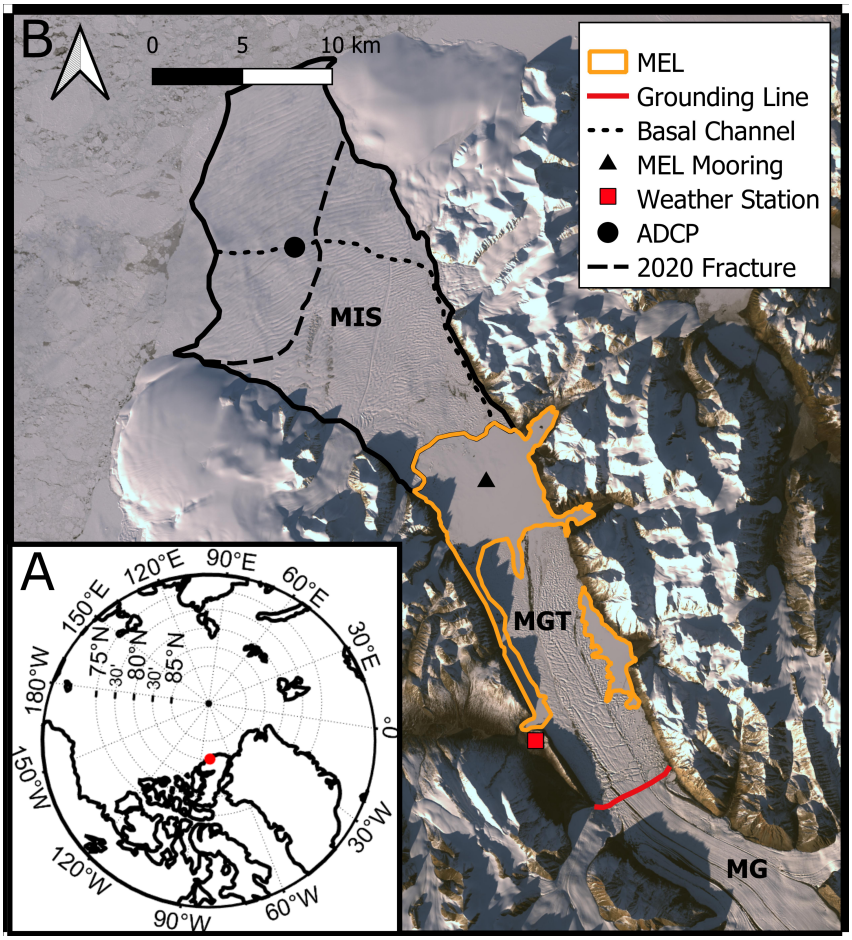

Figure 1. A) Location of Milne Fiord (82.6°N, 81.0°W). B) Landsat 8 image of Milne Fiord taken in September 2018. MEL: Milne Epishelf Lake, MIS: Milne Ice Shelf, MGT: Milne Glacier Tongue, MG: Milne Glacier. MIS calved along the long dash line in July 2020.

is approximately 430 m and the depth near the grounding line of Milne Glacier is 150 m. Tides in Milne Fiord are semidiurnal with an amplitude of ∼10 cm. Tidal baroclinicity was observed in current measurements but was too low to produce shear mixing (Hamilton et al., 2017). The average annual air temperature at sea level is -19°C, with the number of positive degree days (a proxy for surface melting) between 100 and 300 from June 1st to September 1st (Hamilton, 2016). At this high latitude, there is no direct solar radiation from mid-October to the beginning of March. Oceanographic measurements on the Ellesmere Island shelf are extremely sparse. It is however acknowledge that it is a relatively quiet zone with weak currents (J. M. Jackson et al., 2014; Aksenov et al., 2011).

2.2 Milne Glacier and Milne Ice Shelf

MG is over 50 km long and is 4 to 5 km wide. It has a thickness of approximately 150 m at the grounding line (Hamilton, 2016). Downfjord from the grounding line, MGT extends 15 km. The thickness of the MGT decreases rapidly and the ice thickness is less than 10 m at its margins. It broke away from the glacier in 2009 but has not moved significantly since.

Before July 2020, MIS occupied 200 km^2 at the mouth of Milne Fiord. The estimated mean ice thickness was 47 m with a maximum and a minimum around 94 m and 8 m, respectively (Hamilton, 2016; Mortimer et al., 2012). The thinnest area was along a basal channel that runs westward from the east shore (Hamilton et al., 2017; Mortimer et al., 2012; Rajewicz, 2017) (Figure 1). Figure 1 shows the line of fracture where MIS calved at the end of July 2020. Approximately 86 km^2 broke away, including some area where the ice was the thickest (over 80 m). The break up happened during open ocean conditions offshore.

2.3 Milne Fiord Epishelf Lake

From a physical perspective, the most striking feature of the MEL is the extremely sharp salinity interface between the freshwater and the ocean below. The depth of the halocline, taken as the depth of maximum density stratification, is used as a definition of the depth of the epishelf lake (Hamilton et al., 2017).

MEL experiences an annual cycle of deepening and shoaling. Summer is here defined as the period between the first and last day with a least one hour of air temperature over 0°C. Winter is defined as the period between two summers. During the summer, when snow and ice are melting, water from surface runoff flows into the lake deepening the freshwater layer (Figure 2A). Meanwhile, water deeper than the minimum draft of the ice shelf flows to the ocean. When summer is over, surface runoff stops and the lake slowly shoals until summer (Figure 2B). It is thought that the flow of epishelf lake water to the ocean is exclusively along the ice shelf basal channel and is hydraulically controlled by its dimensions (Hamilton et al., 2017; Rajewicz, 2017). This study tests this hypothesis by modeling the outflow during the winter period. Using satellite imagery, it is estimated that MEL covers 71.2 km^2. As a result of short summers, cold long winters and a freshwater cap, the lake is permanently ice-covered. The minimum ice thickness observed was 0.65 m in July 2010 (Hamilton, 2016) and a maximum of 3.19 m was observed in May 1983 (Jeffries, 1985).

3 Data and Methods

3.1 Field Observations

A mooring tethered to the ice was deployed in the center of MEL in May 2011 and has been recording since then. The data from the original deployment to July 2019 are analyzed here. The only time gaps are during fieldwork when the mooring was serviced. Over the years, the mooring configuration changed substantially and different instruments

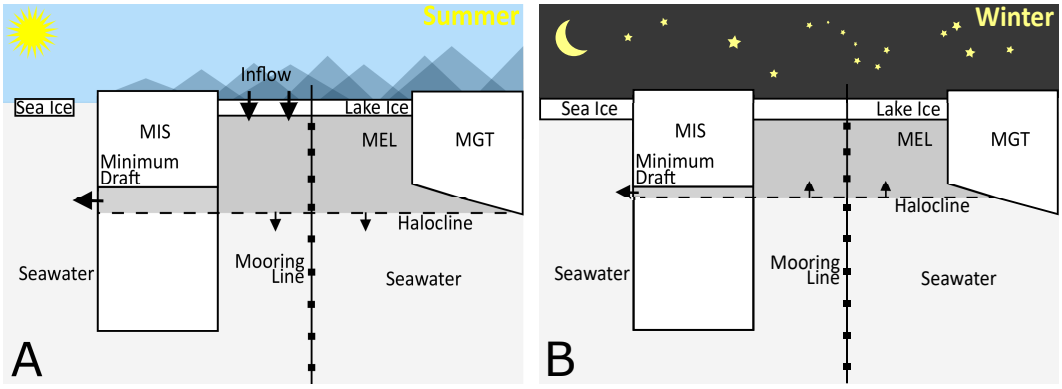

Figure 2. Schematic of Milne Fiord including Milne Ice Shelf (MIS), Milne Epishelf Lake (MEL) and Milne Glacier Tongue (MGT). A) During the melt season (summer) (∼June 1st to ∼September 1st), meltwater inflow drives the deepening of MEL. B) During the remainder of the year, the thickness of MEL decreases slowly toward the minimum draft of the MIS.

have been used. Since the focus here is on annual and interannual variations, data from all the mooring instruments were averaged daily for the following analysis. The accuracy of the moored instruments was superior to ±0.01°C and 0.05 mS cm^{-1} (drift included). When pressure data was available (6 out of 8 years), instrument depth was corrected for shifts in elevation due to ice formation/melting on the lake (0-0.2 m). All temperature and salinity data in this study were converted to the TEOS-10 standard as conservative temperature, Θ [°C] and absolute salinity, S_A [g kg^{-1}] using the GSW oceanographic toolbox (McDougall & Barker, 2011).

Water profiles were taken every summer in MEL. Instruments used for profiling were an Idronaut Ocean304plus (2015-2016) and an RBR XR-620 (2011-2014, 2017-2019). The accuracy of these instruments is ±0.002 °C, ±0.003 mS cm^{-1} and ±0.37 dbar, with a drift of ±0.002 °C a^{-1}, ±0.012 mS cm^{-1} a^{-1}, and ±0.7 dbar a^{-1}. Calibration was done every other year and a crosscheck with other CTD instruments was also performed. Profiles were taken at recovery and deployment of the mooring to crosscheck the mooring instruments and to resolve water properties between them.

A weather station installed next to a small bay in Purple Valley (Figure 1) has been recording hourly data continuously since 2009 (data courtesy: Luke Copland). Data available is temperature, wind (speed and direction), relative humidity, atmospheric pressure and solar radiation. A weather station was also installed on the ice shelf from July 2016 to July 2018. Even though the Purple Valley station is sheltered compared to the ice shelf station, decomposed N-E-S-W winds at ∼2 m show similar direction and speed.

An acoustic doppler current profiler (ADCP) moored near the apex of the ice shelf basal channel (Figure 1) recorded from July 2017 to July 2019. The instrument (Teledyne Workhorse 1200kHz) recorded hourly current measurements using 0.2 m (2017-2018) and 0.25 m (2018-2019) vertical bins. Using the July 2016 channel morphology data from Rajewicz (2017) and the approximated 71.2 km^2 lake area (Hamilton et al., 2017), the data from the ADCP and the model can be compared in order to evaluate the model outflow over the 2016-2017 and 2017-2018 winter deployments.

3.2 Model Formulation

A one-dimensional model (Figure 3) was used to analyze the mooring data during the winter. It is emphasized here that the model was used as a diagnostic tool to examine mixing and the outflow, not as a prognostic one. It was designed to analyze all of the available winter data from the mooring in a simplified context with a small number

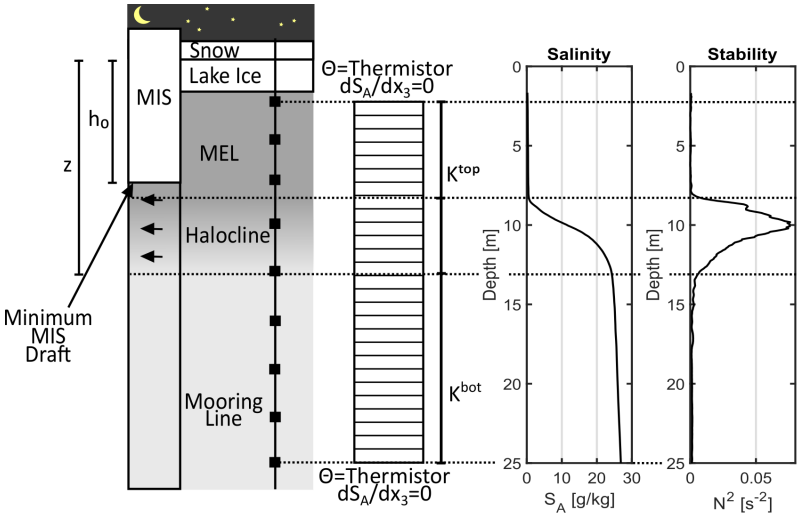

Figure 3. Schematic of the one-dimensional model. Typical absolute salinity and stability profiles are on the right. The data from the uppermost thermistor and the 25 m thermistor are used as boundary conditions for temperature and no-flux boundary conditions are used for salinity. Mixing coefficients of the top freshwater layer (K^{top}) and the bottom seawater layer (K^{bot}) are parameters of the model; only molecular mixing is considered in the halocline layer. The outflow layer is between the minimum draft of the ice shelf (h_0) and the bottom of the halocline layer (z). The top and bottom dashed lines show the top and bottom boundaries of the model. The two middle dashed lines are the top and bottom of the halocline layer (molecular diffusivity only).

of free parameters. The model estimates the vertical mixing in the upper water column and the outflow through the basal channel. In order to do this, the mooring data was employed to determine the parameters of the model using an iterative method.

To model the transport of heat and salt, the Reynolds-averaged transport equation for scalar properties was used (Kundu et al., 2012):

$$\frac{\partial \overline{\varphi}}{\partial t} + \overline{u_j}\frac{\partial \overline{\varphi}}{\partial x_j} + \frac{\partial(\overline{u_j'\varphi'})}{\partial x_j} = K_m \frac{\partial^2 \overline{\varphi}}{\partial x_j^2} \tag{1}$$

Where $\overline{\varphi}$ is a Reynolds-averaged scalar (e.g. conservative temperature or absolute salinity) , $\overline{u_j}$ is the Reynolds-averaged velocity vector and K_m is the molecular diffusivity. t is the time and x is the dimension ($[x_1\ x_2\ x_3] = [x\ y\ z]$, x_3 being in the vertical direction). The following simplifying assumptions were made:

- The average vertical velocity $\overline{u_3}$ is nil ($\overline{u_3} = 0$)
- The horizontal gradients are negligible ($\overline{u_1}\frac{\partial \overline{\varphi}}{x_1} \approx \overline{u_2}\frac{\partial \overline{\varphi}}{x_2} \approx \frac{\partial^2 \overline{\varphi}}{\partial x_1^2} \approx \frac{\partial^2 \overline{\varphi}}{\partial x_2^2} \approx \frac{\partial^2 \overline{u_1'\varphi}}{\partial x_1^2} \approx \frac{\partial^2 \overline{u_2'\varphi}}{\partial x_2^2} \approx 0$)
- Eddy diffusivity can be used to estimate turbulence ($\overline{u_3'\varphi'} \approx -K_t \frac{\partial \overline{\varphi'}}{\partial x_3}$), with K_t representing a turbulent eddy diffusivity

This leads to:

$$\frac{\partial \overline{\varphi}}{\partial t} = K \frac{\partial^2 \overline{\varphi}}{\partial x_3^2} \tag{2}$$

where K is the combined diffusivity ($K = K_t + K_m$), here referred to as the mixing coefficient.

In order to take into account the outflow of the epishelf lake (Figure 3), the basal channel was simplified as a rectangular weir (Figure 4), which allowed the outflow to be described. The model works to estimate four different parameters: two mixing coefficients (K^{top}, K^{bot}, see below) for every day and two annual outflow parameters ($C_e b$, h_0, see below). To find the value of these parameters, these quantities were constrained to a number of possible values and then an iterative method was employed to find the best fitting coefficients using the daily averaged mooring data as the evaluation data set. The model was solved on a 10 cm by 30 minute grid using a Crank-Nicolson finite difference scheme. Grid space and time independence was verified by using different mesh sizes.

3.2.1 Boundary conditions

For temperature, the daily averaged data from the uppermost unfrozen thermistor and the thermistor at 25 m depth were used as Dirichlet boundary conditions at the top and bottom nodes. For salinity, a no-flux ($\partial \overline{S_A}/\partial z = 0$) boundary condition was used. Since mixing is very limited (as will be shown in the results section), no salt flux at 25 m is a reasonable assumption even though gradients do exist at that depth. This is especially true since the focus here is on the epishelf lake.

3.2.2 Initial conditions

The model was reset at the beginning of every winter with new initial conditions. Each run was started when the water temperature in the lake stopped increasing. For temperature, initial conditions were given by a linear interpolation between the mooring instruments. Initial salinity conditions were obtained by using the last CTD cast taken during the field season and fitting this profile to the mooring salinity data by shifting it vertically to get the best fit (minimum RMSE). CTD profiles in July, August and May support this method. Each run was stopped at the first day with positive air temperature to ensure no changes in water properties or mixing from surface meltwater inflow.

3.2.3 Mixing

In order to account for mixing, the water column was divided into three layers (freshwater, halocline and seawater), each with different mixing coefficients (Figure 3). The layer boundaries were defined as the points where the squared Brunt-Visl frequency equaled 10^{-2} s^{-2}. This demarcation is supported by the minimum Richardson number ($Ri = N^2/(\frac{\partial u}{\partial z})^2$) found in the water profile. An observed velocity gradient around 0.01 s^{-1} from Hamilton (2016) and induction current meter measurements (not shown) in combination with perpetual high stratification ($>10^{-2}$ s^{-2}) made it possible to rule-out turbulent mixing in the halocline. However, within the top freshwater and bottom seawater layers, CTD measurements indicate stratification is not strong enough to preclude turbulent mixing. The threshold of 10^{-2} s^{-2} was arbitrarily chosen as it delineates the region of high salinity gradient with good precision in all CTD profiles (Figure 3). To summarize:

- The top layer, from the top boundary to $N^2 = 10^{-2}$ s^{-2} had mixing coefficients for heat (K_Θ^{top}) and salt (K_{SA}^{top}).
- The halocline layer, where $N^2 > 10^{-2}$ s^{-2}, only had molecular diffusion.
- The bottom layer, from $N^2 = 10^{-2}$ s^{-2} to the bottom boundary, had mixing coefficients for heat (K_Θ^{bot}) and salt (K_{SA}^{bot}).

Values of 1.4x10^{-7} m^2 s^{-1} and 1.4x10^{-9} m^2 s^{-1} were employed for molecular diffusivities of heat and salt, respectively (P. R. Jackson & Rehmann, 2014). Possible K_Θ coefficients were: [1.4, 2, 4, 8, 16, 32, 64, 128, 256, 512, 1024]x10^{-7} m^2 s^{-1}. The power of two incre-

ment was chosen to reasonably cover orders of magnitude from 10^{-7} to 10^{-4} for K_Θ while keeping the required computational power reasonably low (typical laptop). The upper limit of 1024x10^{-7} m^2 s^{-1} was chosen as K_Θ only very rarely reaches this value (as will be shown in the presented results).

As first pointed out by Turner (1968), when turbulence is weak, the mixing of heat and salt is not the same (i.e. the turbulent Lewis number ($Le = \frac{K_{t,\Theta}}{K_{t,SA}}$) is not one). Differential diffusion (Le≠1) has been observed in the ocean and demonstrated in laboratory and numerical experiments (Gargett, 2003). Because Milne Fiord is a quiet environment, it is important to take into account differential diffusion in order to model the water column properly. To account for this phenomenon, the parameterization of P. R. Jackson and Rehmann (2014) was applied to link K_Θ^{top} to K_{SA}^{top} and K_Θ^{bot} to K_{SA}^{bot} and reduce the number of unknowns. Using the ratio determined by these authors, possible K_{SA} coefficients were: [0.0014, 0.002, 0.004, 1.5, 4.3, 12, 33, 81, 191, 425, 915]x10^{-7} m^2 s^{-1}.

3.2.4 Outflow

Assuming most of the water outflow is through the basal channel in the ice shelf and that it can be simplified as a rectangular channel (Hamilton et al., 2017), the outflow was modelled based on an inverse rectangular weir equation (Kindsvater & Carter, 1959) (Figure 4):

$$\frac{d(z-h_0)}{dt} = \frac{2}{3A_{lake}}\sqrt{2g'}C_e b(z-h_0)^{2/3} \tag{3}$$

Where h_0 is the depth of the minimum draft of the ice shelf, C_e is a friction coefficient, b is the width of the rectangular channel, z is the depth at the bottom of the outflow layer and A_{lake} is the area of the lake ($\sim$ 71.2x10^3 m^2). g' is the reduced gravity ($\frac{g\triangle\rho_0}{\rho} \approx 0.25$ m s^{-2}), where g is the gravitational acceleration, $\triangle\rho$ is the density difference between the freshwater and the seawater (25 kg m^{-3}) and ρ is a reference density (1000 kg m^{-3}). $C_e b$ and h_0 are two unknown parameters that were assumed constant for the duration of each winter. $\frac{d(z-h_0)}{dt}$ was computed every day and the amount of water flowing out to the ocean was modeled by shrinking the outflow layer (i.e. $z-h_0$ was reduced). This assumes that the outflow velocity is the same everywhere in the outflow layer. The above simplifications were derived from current measurements and ice penetrating radar measurements over the channel (Rajewicz, 2017). In order to compensate for the outflow, water was added at the bottom of the model using the properties of the bottom node. Using equation 3, possible values for h_0 ranged from 3 to 10 m. The possible values for $C_e b$ ranged from 2 to 10 m, which gives a minimum channel width from 2.5 to 18 m using common rectangular weir coefficients (0.55 to 0.8) (Hamilton et al., 2017).

3.3 Model Fitting

In order to find the optimal model parameters, an iterative scheme was employed. A custom coefficient of agreement (C_a) was used to enable Boolean comparison between iterations. All mooring instruments in the top 25 m were used for the calibration. For the temperature calibration, the model output was compared to the linearly interpolated data at every grid node and the root mean squared error ($RMSE_{\Theta,model}$) was computed and then normalized by the standard deviation of daily averaged and linearly interpolated mooring data ($STD_{\Theta,mooring}$). For the salinity data, the model output was linearly interpolated to the precise depth of each salinity instrument, then the root mean squared error ($RMSE_{SA,model}$) was computed and normalized by the standard deviation of the salinity data ($STD_{SA,mooring}$). The temperature score $\left(\frac{RMSE_{\Theta,model}}{STD_{\Theta,mooring}}\right)$ and the salinity score $\left(\frac{RMSE_{SA,model}}{STD_{SA,mooring}}\right)$ were weighted to take into account the number of temperature measurements (n_T) and conductivity measurements (n_C). For example, if there were 10 temperature data points and four conductivity data points on the mooring line, the temperature score was weighted by 10/(10+4) and the salinity score was weighted by 4/(10+4).

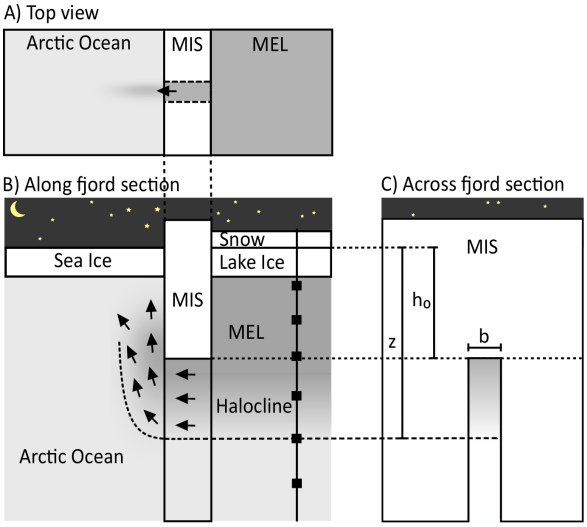

Figure 4. Schematic of the outflow of the lake through the basal channel of the ice shelf. A modified weir equation using a two layer simplification (equation 3) is used to constrain the number of parameters related to the outflow. A) Top view. B) Along fjord section. C) Across fjord section through MIS. Note: not to scale

To summarize, the C_a was computed with the following equation:

$$C_a = \left(\frac{n_T}{n_T + n_c} \left(\frac{RMSE_{\Theta,model}}{STD_{\Theta,mooring}} \right) + \frac{n_c}{n_T + n_c} \left(\frac{RMSE_{SA,model}}{STD_{SA,mooring}} \right) \right)^{-1} \tag{4}$$

The normalization by the standard deviation of the mooring data allowed combination of temperature and salinity data by placing them on a similar scale. The weights allowed combination of these evaluation scores by adjusting their importance according the respective number of measurements. The -1 exponent was used to yield a positive relationship between C_a and the model skill (i.e. a high C_a means a good agreement). A value around 1 would indicate that the model performed poorly, since the $RMSE$ would have the same magnitude as the STD (basically random). On the other hand, a value of 10 would mean the model was very skillful since the $RMSE$ would be 10 times smaller than the STD.

Figure 5 is a schematic of the iterative model calibration workflow. The first step was to write the boundary and initial conditions into the model mesh (1). Then, a pair of outflow coefficients ($C_e b$ and h_0) was selected in order to calculate the daily outflow throughout the winter (2). Next, the mixing coefficients returning the highest C_a were found for day 1 (3-6). Steps 4-6 were repeated for every consecutive day. Once the daily mixing coefficients were determined, the C_a for the whole winter was computed (7) and steps 2-7 were repeated, narrowing down on the optimal $C_e b$ / h_0 pair. Finally, the pair of outflow coefficients returning the highest C_a for the whole winter was selected as the best fitting parameters. This procedure was repeated for the remaining seven winters of mooring data (2011-2019). The model version with the best fitting parameters for each winter was used to generate the output in the Results section.

4 Model Results and Validation

4.1 Temperature

Figure 6A shows the daily averaged and linearly interpolated mooring data. The annual cycle of deepening and shoaling of MEL is clearly visible, as is the sharp temper-

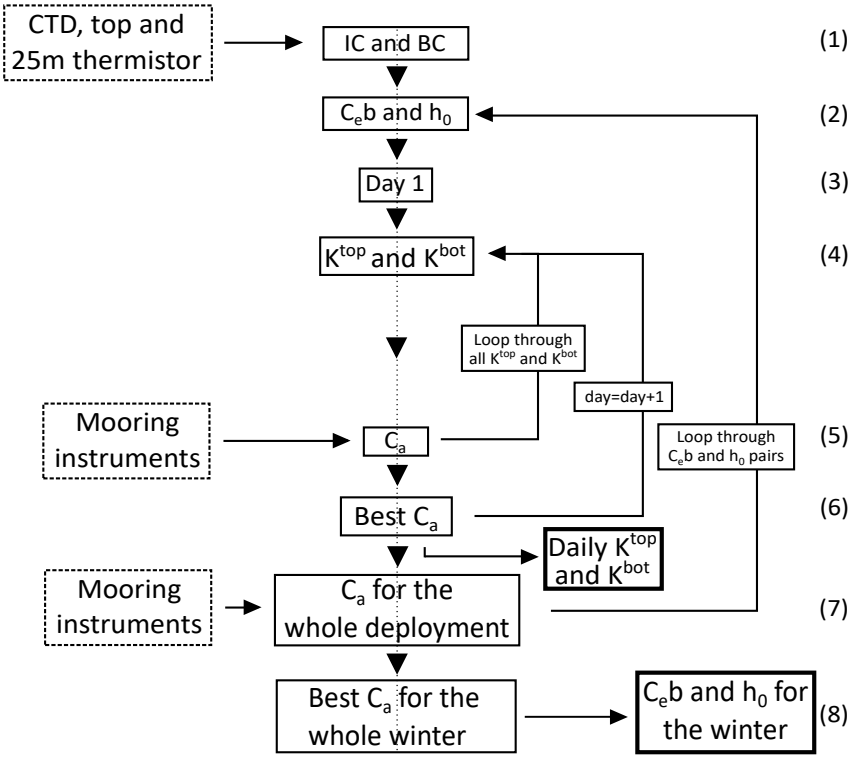

Figure 5. Once the initial conditions (IC) and the boundary conditions (BC) are implemented into the mesh, the model loops through the possible outflow coefficients ($C_e b$ and h_0) for every winter and through the possible mixing coefficients for every winter day. (See text for detailed explanation)

ature gradient is associated with the halocline. The maximum temperature in MEL is reached around mid-August and decreases until the following summer. The temperature of the water below the halocline is far less variable than the temperature above the halocline.

Temperature output from the model (Figure 6B) agrees well with the temperature data from the mooring (RMSE=0.19°C, STD=0.17°C, r^2=0.97, bias=0.067°C). Figure 6C shows the difference between the model and the linearly interpolated mooring data. The model output appears as a smoothed version of the mooring data, which demonstrates that the main seasonal physical characteristics are reproduced. Three main differences can be observed between the model and the mooring data. First, the temperature oscillations (period around 10 days) above the halocline present in the mooring data are not reproduced in the model. Since there is no significant addition of heat from vertical processes during the winter, these oscillations must be the result of advection of horizontal temperature gradients, which are not considered in the model. The second major disparity is found near the halocline where slight deviations in the modeled halocline depth result in substantial temperature errors because of the sharp gradient at this location. This type of error is due to the simplified consideration of the outflow in the model, which is held constant for the whole winter. The last major difference is the inflow of cold water between 15 m and 22 m in the mooring data of 2015-2016 and 2016-2017 (Figure 6A). This increased the error for the bottom part of the water column for many months. These main differences between the model and the mooring data are the result of the simplifications made in the model (one-dimension, no advection, rectangular weir outflow). However, considering the visual and statistical agreement, the model is considered appropriate for the study of the full winter timeseries.

4.2 Salinity

The agreement between the model and the mooring salinity data is inferior to that for temperature, but the model still fits the main characteristics of the salinity profile in the fjord (Figure 7). The average RMSE is 2.0 g kg^{-1}, the standard deviation is 1.7 g kg^{-1} and the bias is 1.1 g kg^{-1}. The main discrepancies are found in the top of the water column where the model tends to diffuse more salt into the freshwater than the mooring instruments indicate. This is because the simulated halocline is compressed in the outflow process, increasing the salinity gradient to values higher than observed in situ. Since the salt flux is proportional to the gradient, more salt makes its way to the top layer as a result of this artifact. Nonetheless, the model shows the main features of the epishelf lake which are a freshwater layer atop a sharp halocline that moves upwards during the winter.

4.3 Outflow

The depth of the halocline (bottom of the epishelf lake) returned by the model is shown in Figure 8A, as well as the outflow parameters for each year (legend). The trajectories of the halocline from 2014 to 2019 are closely grouped but the first two years of the record (2011-2012 and 2012-2013) exhibit a more pronounced shoaling. The minimum draft of the ice shelf (h_0) returned by the model is similar for every year (between 6.7 and 7.9 m) except for the 2015-2016 year (5.3 m). The outflow friction-width coefficient ($C_e b$) varies more but stays within the range of realistic values. There are no perceptible trends in either $C_e b$ or h_0.

Figure 8B shows the approximated flow rate through the channel according to the model (dashed lines) and the moored ADCP (solid lines). The total discharge of 2.0x10^8 (2017-2018) and 2.3x10^8 m^3 (2018-2019) for the model and 1.4x10^8 (2017-2018) and 0.9x10^8 m^3 (2018-2019) for the ADCP are similar.

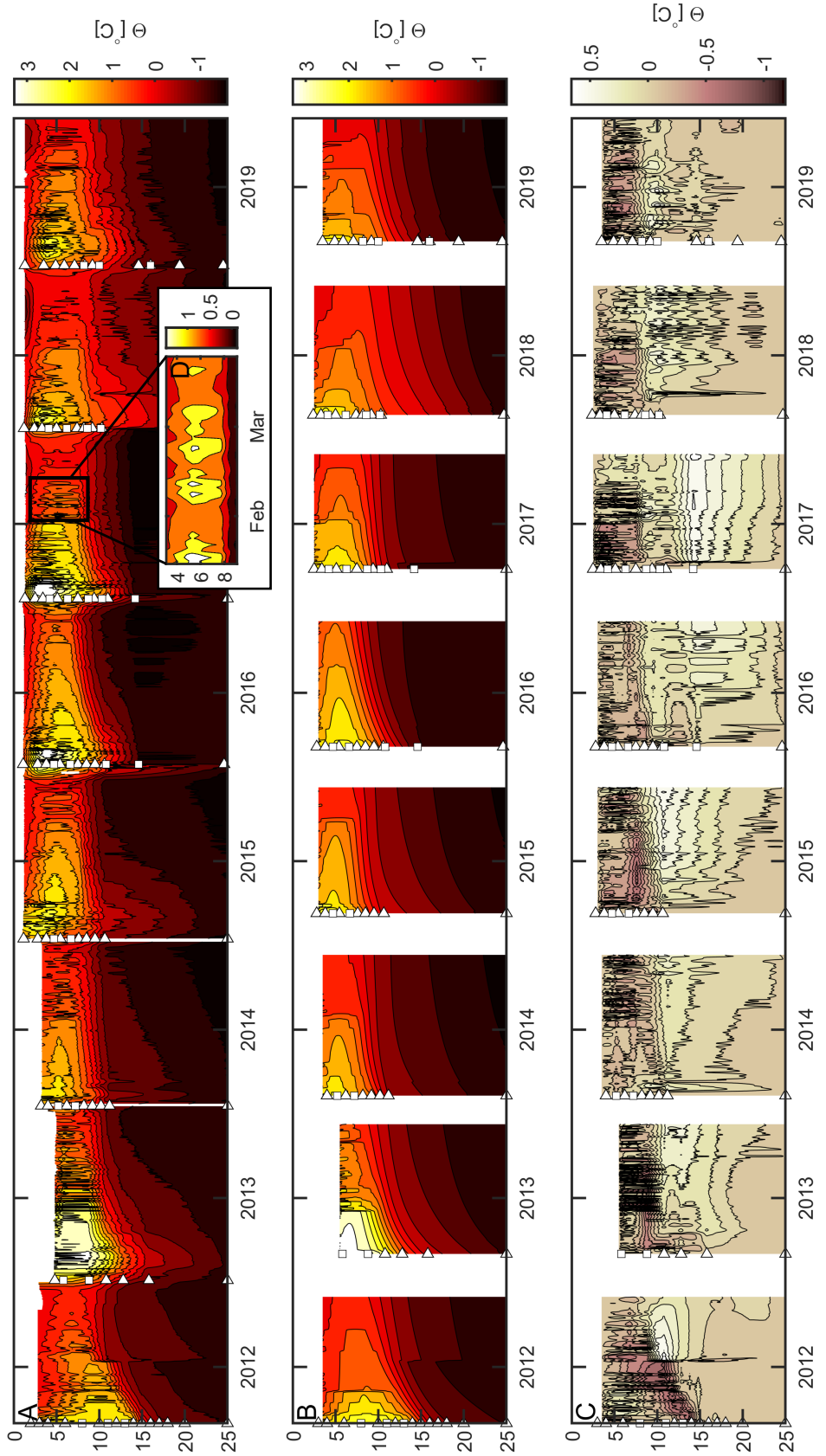

Figure 6. Temperature timeseries of the top of the water column in Milne Fiord. A) Temperature timeseries from the mooring (linearly interpolated). B) Temperature timeseries from the model. C) Difference between the model and the mooring data, positive values mean the model temperature is higher than the mooring temperature. Triangles show the location of the thermistors on the mooring line and the squares show the location of the conductivity instruments. D) Temperature oscillations close-up.

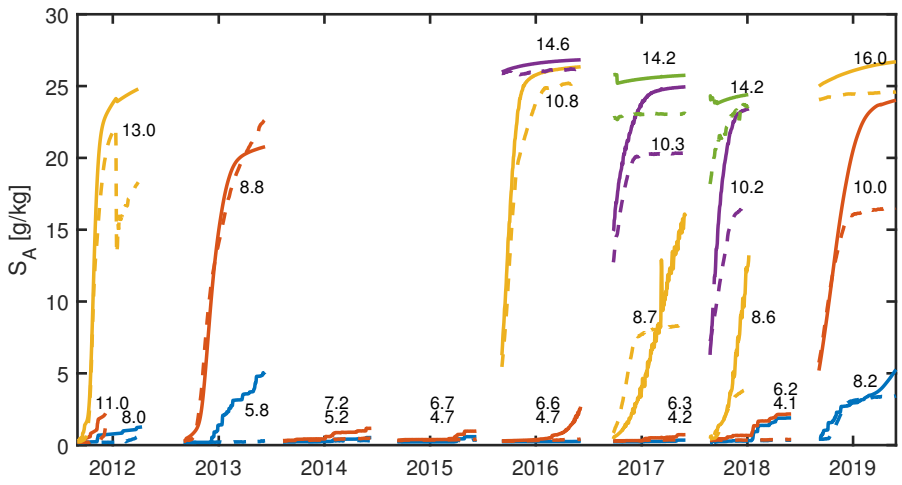

Figure 7. Salinity data from the model (solid line) at the depth of the conductivity instruments on the mooring (dashed line). Labels are the depth of the instruments, in meters.

4.4 Mixing

The daily mixing coefficients returned by the model are shown by the dots in Figure 9. The solid lines represent a 30 day moving average of apparent thermal diffusivity. The top layer of freshwater above the halocline experiences more mixing than the seawater below except during the first months (September and October) after the melt season. The total amount of mixing in the top of the water column differs greatly from year to year, with a minimum winter average of $2.5\text{x}10^{-7}$ m^2 s^{-1} in 2015-2016 and maximum $1.2\text{x}10^{-5}$ m^2 s^{-1} in 2018-2019. The mixing below the halocline is more uniform, spanning from $1.8\text{x}10^{-7}$ m^2 s^{-1} in 2015-2016 to $2.3\text{x}10^{-6}$ m^2 s^{-1} in 2013-2014.

If the model was over-mixing, the heat content of the freshwater layer would be lower in the model than in the mooring data, as a higher K_Θ^{top} implies a higher heat flux out of the top layer. Analysis of the heat content in the top freshwater layer shows that the model does not over- or under-mix, increasing the confidence in the results.

5 Discussion

5.1 Numerical Model

The one dimensional model employed in this study was shown to reproduce well the characteristics of the winter mooring data in Milne Fiord. It enables the description of the main physical mechanisms using only four different parameters. Consequently, these parameters can be examined in order to get a better understanding of Milne Fiord system. The iterative technique developed here could be used to investigate other systems that have mooring data.

5.2 Outflow

Outflow estimated from the ADCP data and the model agree well for 2018-2019, but there is significant divergence from late November 2017 to summer 2018. An event at the end of November 2017 resulted in a substantial increase in outflow velocity out of the fjord. Moreover, Figure 8B shows that the outflow remained higher following this outflow event, following the same trend as the model but with higher values. Unfortu-

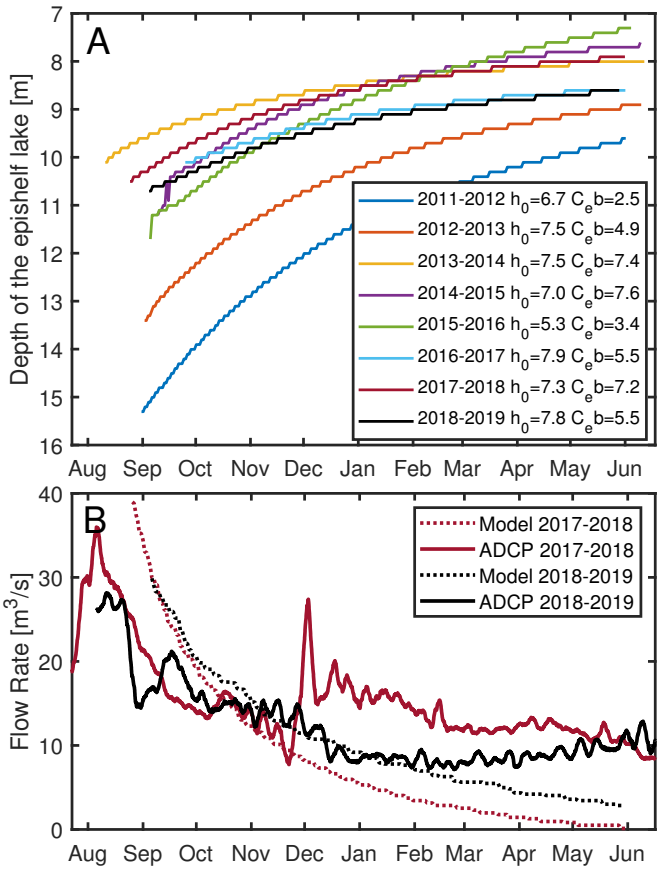

Figure 8. A) Depth of MEL (maximum N^2 value) given by the model for each winter. The staircase effect is due to the vertical discretization of the model (10 cm). Best fit outflow parameters h_0 and $C_e b$ for each winter are in the legend. B) Outflow through the basal channel in MIS. Dotted lines are the model estimation using the rectangular weir equation and an estimated lake area of 71.2 km^2. Solid lines are the ADCP outflow estimation using a 10 day moving average.

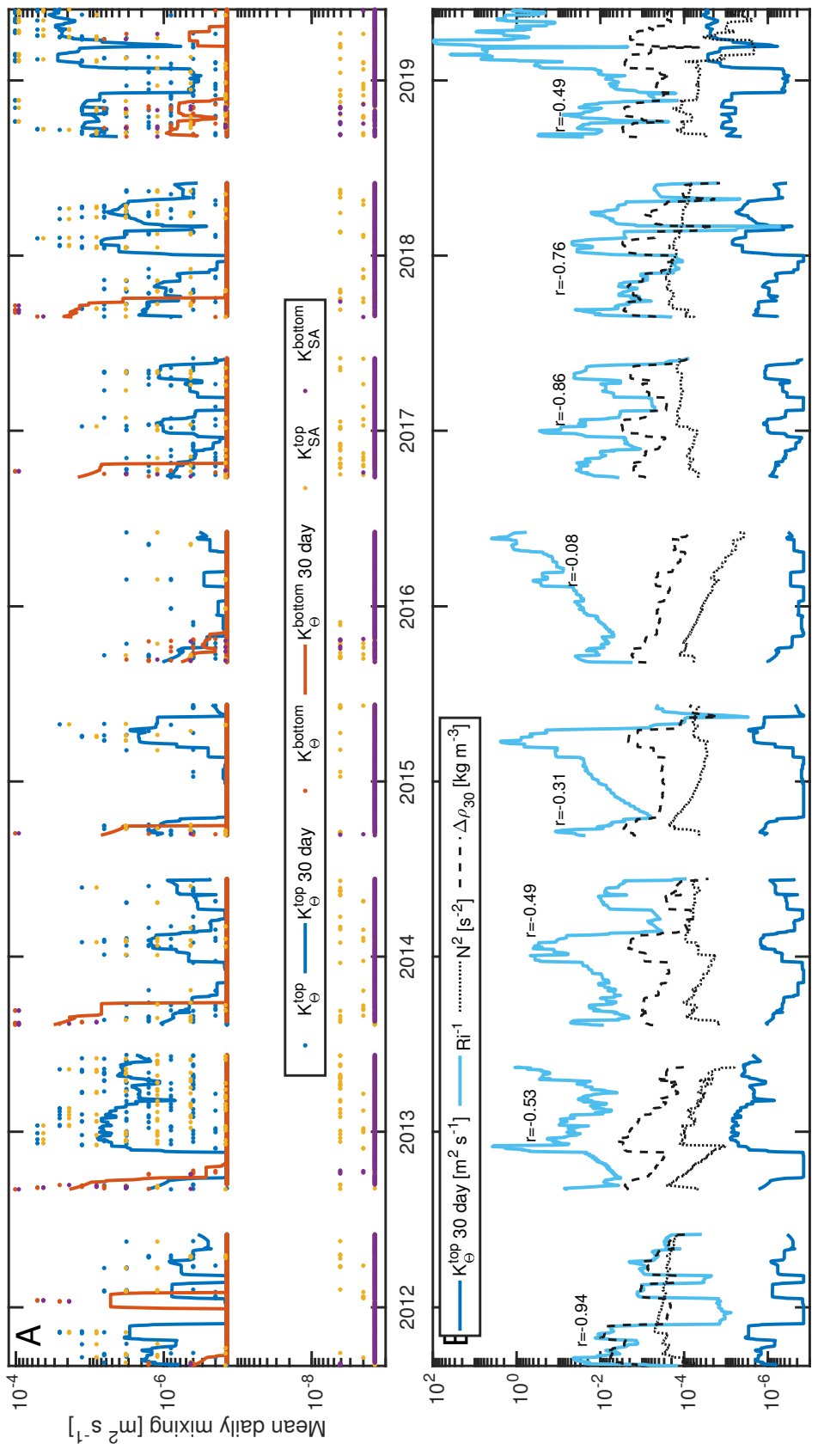

Figure 9. A) Daily mixing coefficients from the model, for the heat and salt transport equations for the top and bottom layers (dots). Solid lines are the 30 day averaged quantities for the top (blue) and bottom (red/orange) coefficients of the heat equation. Minimum possible values of daily mixing coefficients are the molecular diffusivities; $1.4\text{x}10^{-7}$ m^2 s^{-1} for heat and $1.4\text{x}10^{-9}$ m^2 s^{-1} for salt. B) 30 day averaged mixing coefficient (dark blue) and inverse of the Richardson number (light blue) computed according to equation 6. N^2 (dotted line) computed by the model and 30 day maximum density difference attributed to the temperature oscillations $\triangle\rho_{30}$ (dashed line) are used in equation 6. All values are for the top layer. Enhanced mixing (dark blue line) is linked to stronger eddy activity (dashed line) hence to a lower Richardson number (light blue line). The correlation coefficient (r) between Ri and mixing for each winter is above the Ri^{-1} line.

nately, it has not been possible to determine what caused this abrupt acceleration event captured by the ADCP. The ADCP flow rate in Figure 8B is estimated assuming the vertical velocity profile is constant across the cross section of the channel and assuming the channel cross section at the location of the ADCP did not change over time. These two assumptions are approximate, but this is the only way to compare in situ data with the model outflow. Considering its rough character, the comparison between the model results and the ADCP data is an order-of-magnitude type comparison. Since the trends are similar and the bulk outflow quantities match reasonably well; it is therefore conclude that they agree. Moreover, the model C_a is no worse in 2017-2019 than for the other years. This suggests the velocity increase, as experienced by the ADCP, is not directly linked to the epishelf lake.

The agreement between the model and the observations is not enough on itself to prove conclusively that the basal channel is the only outflow for the epishelf lake water. However, since the ADCP outflow is similar to the model and that ice penetrating radar measurements did not detect another probable path for outflow; it is reasonable to infer that the basal channel taken into account in this study is the main outflow path.

Channels under ice shelves and glacier tongues have attracted attention in recent years (e.g. Le Brocq et al., 2013; Alley et al., 2016; Dow et al., 2018). Buoyant water from subglacial melt and discharge converge in these longitudinal ice depressions, concentrating the melting in the channel apex (Millgate et al., 2013; Rignot & Steffen, 2008). Many recent studies estimated basal channel melt rates (Stanton et al., 2013; Dutrieux et al., 2013; Gourmelen et al., 2017; Alley et al., 2016), all agreeing that these locations experience enhanced melt (i.e. negative ice mass balance). For the present study, the outflow parameters of the model lead to the conclusion that the minimum draft of the ice shelf has not experienced a major change between September 2011 and July 2019. Indeed, if the melting was continuous in the channel, there would be a trend in the outflow coefficients. For example, h_0 would decrease year after year if the apex of the channel was continuously thinning, but this is not the case. The fact that h_0 went from 7.0 m (2014-2015) to 5.2 m (2015-2016) then up to 7.9 m (2016-2017) implies that the apex of the channel at the main constriction is in neutral mass balance over a multi-year time scale. Likewise, the fact that $C_e b$ does not show any particular trend also points towards a multi-year equilibrium in ice mass along the channel. This agrees with past evidence of ice accretion under Ward Hunt Ice Shelf (100 km to the east) (Jeffries et al., 1988). This result shows that the MIS basal channel is not necessarily an area of concentrated ice loss over a multi-year time scale. Although water at the apex of MIS channel is from a different source (epishelf lake) than the water at the apex of other ice shelf channels (buoyant plume from melting), this result is in marked contrast to what is found in the literature at other locations (Rignot & Steffen, 2008; Stanton et al., 2013; Dutrieux et al., 2013; Alley et al., 2016), but in agreement with Gladish et al. (2012) who show that basal channels may act to stabilize ice shelves. The calving of 45% of the MIS in July 2020 occurred along existing rifts but transverse to the channel (Figure 1). This suggests that the basal channel did not play a role in the break-up.

5.3 Mixing

Mixing during the first part of the winter (September-October) occurs both above and below the halocline. For the seawater layer, wind data from the Purple Valley weather station (2011 to present) and from a weather station on the ice shelf (2016-2018) shows that along-coast (NE) winds are low during the whole year except from July to September. If a shore lead is present or if the wind stress drives sea ice movement (Williams et al., 2006), coastal upwelling is expected to happen during these NE wind episodes. Examination of the 50 m thermistor shows a deflection of isotherms during these periods (not shown). It is then suggested that mixing occurring below the halocline just after the end of the melt season is linked to coastal upwelling, similar to R. H. Jackson et al. (2014). Other shelf processes (e.g. coastal trapped waves (Inall et al., 2015)) and fjord

processes (e.g. buoyancy driven circulation (Carroll et al., 2015)) possibly play a role below the epishelf lake. However, the focus here is on the epishelf lake. Aside from a peak in January 2012 and April 2019, mixing below the halocline is at molecular levels (K_Θ=1.4x10^{-7}m^2 s^{-1}) for the entire time after the residual summer mixing vanishes.

The mixing estimates given here are the first for an epishelf lake. There are very few quantitative estimates of mixing in ice-covered lakes, especially during winter when the effect of solar radiation is removed. Hence, the results presented here are particularly relevant to all low energy ice-covered water bodies at high latitude and mid-latitude lakes that experience substantial snow-cover. Although the average winter mixing coefficient for heat in MEL (2.5x10^{-6} m^2 s^{-1}) is small relative to what is typical in lakes (e.g. Lin et al., 2020) or in the adjacent Arctic Ocean (e.g. Chanona et al., 2018), it is ∼20 times larger than the rate of molecular diffusion. This means heat fluxes ∼20 times higher, with an even greater impact on other tracers such as salinity or dissolved oxygen, as their molecular diffusion rate is lower.

Without wind or solar radiation, with minimal tides and an ice cover, the processes leading to mixing above the halocline are very limited in winter. Comparison of the temperature profile and salinity of the top layer (∼0.2 g kg^{-1}) with studies on salt exclusion (Pieters & Lawrence, 2009; Bluteau et al., 2017) does not indicate this process could play an important role, especially over the entire winter. Moreover, in depth analysis of the meteorological data did not reveal correlation between mixing events and any of the available variables (temperature, wind, radiation, snow depth, atmospheric pressure). This demonstrates the isolating characteristic of the ice and snow cover.

On the other hand, examination of the water temperature timeseries shows that enhanced mixing is linked to the presence of 7 to 30 day oscillations in the temperature signal (Figure 6D). Because there is no addition of heat to the lake during winter, these temperature oscillations can only be due to advection of horizontal temperature gradients in MEL. Comparison of the temperature oscillations with internal waves seen in lakes and fjords did not yield any insights on their origin. However, the way heat appears and separates isotherms at ∼5 m is reminiscent of horizontal eddies found in the Arctic Ocean (e.g. Hunkins, 1974; Timmermans et al., 2008) or in lakes (e.g. Kouraev et al., 2016; Forrest et al., 2013). Eddies are defined here as circular currents, in or close to geostrophic balance.

In order to link the temperature oscillations in the mooring data to possible eddies and to mixing, the thermal wind equation is used to calculate the vertical shear from the horizontal density gradient (Kundu et al., 2012) :

$$\frac{\partial u_1}{\partial x_3} = \frac{g}{\rho_0 f}\frac{\partial \rho}{\partial x_2} \tag{5}$$

Where f is the Coriolis frequency (1.45x10^{-4} s^{-1} at 82.6°N). The thermal wind equation is then employed to scale the Richardson number:

$$Ri = \frac{N^2}{\left(\frac{\partial u_1}{\partial x_3}\right)^2} \approx \frac{N^2}{\left(\frac{g}{\rho_0 f}\frac{\partial \rho}{\partial x_2}\right)^2} \approx \frac{N^2}{\left(\frac{g}{\rho_0 f}\frac{\triangle \rho_{30}}{R_L}\right)^2} = \left(\frac{N^2 \rho_0 H}{g \triangle \rho_{30} \pi}\right)^2 \tag{6}$$

Where the Rossby radius of deformation ($R_L = NH/f \sim 500$ m) is used to scale the horizontal span of the eddies. N^2 is computed with the model results. The vertical height scale (H) is taken as the distance between the bottom of the ice cover and the point where N^2 becomes larger than 0.01 s^{-2}. Finally, $\triangle\rho_{30}$ is the 30 day maximum density variation related to the temperature oscillations. It is calculated using the mooring temperature data, assuming that the mooring captures the full range of the temperature anomalies (eddies) during a 30 day interval. The temperature oscillations (period of 7 to 30 days) from the mooring data have a greater amplitude than the 30 day temperature difference given by the model (i.e. $\triangle T_{30}^{mooring} > \triangle T_{30}^{model}$) which gives confidence that $\triangle\rho_{30}$ is attributable to horizontal movements (i.e eddies moving around). This is because there is no addition of heat in the epishelf lake, hence, a temperature increase seen by the mooring is a consequence of advection. Moreover, it is acknowledged that the model has higher

mixing coefficients when it encounters temperature oscillations because of the fitting method employed. However, consistently high mixing coefficients (30 day average) are undeniably related to increased vertical mixing.

Figure 9B shows the average Richardson number in the epishelf lake as well as the vertically averaged quantities used for its calculation (N^2 and $\triangle\rho_{30}$) and the 30 day averaged mixing coefficient for heat in the top layer returned by the model (K_Θ^{top}). Peaks in $\triangle\rho_{30}$ are definitely correlated with increased mixing. Simple linear correlation between $log_{10}(\Delta\rho_{30})$ and $log_{10}(K_\Theta^{top})$ gives a correlation coefficient (r) of 0.49 with a p-value $\ll 10^{-5}$. This means that mixing is higher when the temperature oscillations (advection) are present. Figure 9B also shows that peaks in the inverse Richardson number (Ri^{-1}) and mixing in the epishelf lake (K_Θ^{top}) are correlated. r is -0.43 and the p-value $\ll 10^{-5}$ between $log_{10}(Ri)$ and $log10(K_\Theta^{top})$ for the eight winters. The r value for each winter is in Figure 9B. Considering the thermal wind equation and the Rossby radius were used to scale Ri, correlation between the Ri and K_Θ^{top} means the phenomena linking mixing to the temperature oscillations is geostrophic by nature.

Similar results were obtained in the Arctic Ocean, where eddies in geostrophic balance were found to increase vertical diffusivity by about one order of magnitude (Pnyushkov et al., 2018). Equation 6 can also be used to estimate horizontal velocities of around 1 cm s^{-1}. This is similar to that reported in ice-covered lakes (Forrest et al., 2013; Bengtsson, 1996; Huttula et al., 2010) and what an ADCP measured in MEL in May 2011 (Hamilton, 2016).

As previously mentioned, sources of energy in the epishelf lake are very limited during winter. Because mixing does not show any tendency to decrease after the end of the melt season, something has to be energizing the lake motion throughout the winter. Estimation of the Ekman spin down time $t_E = D/(\sqrt{2Kf})$ (Pedlosky, 2013) with the height of the eddies $D \approx 8$ m and the eddy viscosity $K \approx 10^{-6}$ m^2 s^{-1}, gives a time scale around 5 days. This is obviously too short to attribute the existence of the eddies to residual energy from summer processes. The tidal amplitudes in Milne Fiord are very small ($\sim$10 cm) and no tidal signal can be seen in the top thermistors. It is then quite unlikely that tides have an impact on the epishelf lake. Looking at other ice-covered lakes, numerical modeling of Lake Untersee (Antarctica) has shown that the presence of an ice wall created a gyre in winter due to the change of water properties following ice-water interactions (Steel et al., 2015). Since the main body of MEL is bordered by ice upfjord and downfjord (Figure 1), cooling of epishelf lake water due to ice melting could possibly lead to density gradients large enough to drive circulation and form eddies. This would explain the presence of the eddies (and enhanced mixing) throughout winter. Correspondingly, baroclinic instability is thought to be one of the main formation mechanism for eddies in the Arctic Ocean (Pnyushkov et al., 2018; Zhao et al., 2014).

6 Conclusion

Here we have used a one-dimensional model to analyze the winter mooring data of the top water column in Milne Fiord from 2011 to 2019. Three major results stand out from the analysis.

1. The model outflow rates, together with two years of ADCP data and ice penetrating radar surveys, show that the main outflow path for the epishelf lake water is likely through a basal channel under the ice shelf. This can be exploited in hydrological studies of Milne Fiord watershed.
2. The model outflow coefficients indicate that the basal channel area is in ice mass equilibrium over a multi-year time scale. This contradicts most studies of basal channels which state that these ice features are usually rapidly evolving (e.g. Gourmelen et al., 2017; Alley et al., 2016). Our results imply that basal channels are not necessarily linked to active destabilization, and that further investigation of ocean

properties within individual channels are required to better understand their time-evolving nature and potential role in ice shelf breakup.

3. The model mixing coefficients reveal that mixing is greater in the epishelf lake than in the seawater below the halocline. Enhanced mixing in the epishelf lake is linked to temperature oscillations with periods from 7 to 30 day. Moreover, estimation of the Richardson number suggests that enhanced mixing in the epishelf lake is linked to one or more geostrophic wave-like structures (eddies). This demonstrates that low energy physical processes can play a significant role in isolated settings such as epishelf lakes, but also other lakes and fjords experiencing a significant ice cover and limited external forcing.

Acknowledgments

The authors would like to express their gratitude to the following funding agencies: Natural Sciences and Engineering Research Council of Canada (JB: CGSM-6563, BEL: NRS-2018-517975; RGPIN-2018-04843, DM: NRS-2011-402314; RGPIN-2016-06244), the Polar Continental Shelf Program (DM: 604-12; 626-13; 651-14; 642-15; 636-16; 647-17; 627-18; 651-19), les Fonds de Recherche Nature et Technologies du Qubec (JB: 270157), the Northern Scientific Training Program (JB), ArcticNet: GO-Ice: Glacier-Ocean-Iceberg Dynamics in a Changing Canadian Arctic, Impacts of the Changing Global Environment at Nunavuts Northern Frontier, Freshwater resources of the Eastern Canadian Arctic (DM, AKH, JB), Canada Foundation for Innovation (DM: 31410) and the Ontario Research Foundation (DM: 31410). We are also thankful for the logistical support given by the Polar Continental Shelf Program and we would like to thank all the individual who took part in field campaigns in Milne Fiord over the years. The data used in this study is publicly available through the Polar Data Catalogue (CCIN 12101 and 12102; https://polardata.ca/).

References

Aksenov, Y., Ivanov, V. V., Nurser, A. G., Bacon, S., Polyakov, I. V., Coward, A. C., ... Beszczynska-Moeller, A. (2011). The Arctic circumpolar boundary current. *Journal of Geophysical Research: Oceans*, *116*(C9).

Alley, K. E., Scambos, T. A., Siegfried, M. R., & Fricker, H. A. (2016). Impacts of warm water on Antarctic ice shelf stability through basal channel formation. *Nature Geoscience*, *9*(4), 290–293.

Bengtsson, L. (1996). Mixing in ice-covered lakes. *Hydrobiologia*, *322*, 91–97.

Bennike, O., & Weidick, A. (2001). Late Quaternary history around Nioghalvfjerdsfjorden and Jøkelbugten, North-East Greenland. *Boreas*, *30*(3), 205–227.

Bluteau, C. E., Pieters, R., & Lawrence, G. A. (2017). The effects of salt exclusion during ice formation on circulation in lakes. *Environmental Fluid Mechanics*, *17*(3), 579–590.

Carroll, D., Sutherland, D. A., Shroyer, E. L., Nash, J. D., Catania, G. A., & Stearns, L. A. (2015). Modeling turbulent subglacial meltwater plumes: Implications for fjord-scale buoyancy-driven circulation. *Journal of Physical Oceanography*, *45*(8), 2169–2185.

Chanona, M., Waterman, S., & Gratton, Y. (2018). Variability of internal wave-driven mixing and stratification in Canadian Arctic shelf and shelf-slope aters. *Journal of Geophysical Research: Oceans*, *123*(12), 9178–9195.

Dow, C. F., Lee, W. S., Greenbaum, J. S., Greene, C. A., Blankenship, D. D., Poinar, K., ... Zappa, C. J. (2018). Basal channels drive active surface hydrology and transverse ice shelf fracture. *Science Advances*, *4*(6), eaao7212.

Dutrieux, P., Vaughan, D. G., Corr, H. F., Jenkins, A., Holland, P. R., Joughin, I., & Fleming, A. (2013). Pine Island Glacier Ice Shelf melt distributed at kilometre scales. *The Cryosphere*, *7*, 1543–1555.

Forrest, A. L., Laval, B. E., Pieters, R., & SS Lim, D. (2013). A cyclonic gyre in an

ice-covered lake. *Limnology and Oceanography*, *58*(1), 363–375.

Gargett, A. E. (2003). Differential diffusion: An oceanographic primer. *Progress in Oceanography*, *56*(3-4), 559–570.

Gibson, J. A., & Andersen, D. T. (2002). Physical structure of epishelf lakes of the southern Bunger Hills, East Antarctica. *Antarctic Science*, *14*(3), 253–261.

Gladish, C. V., Holland, D. M., Holland, P. R., & Price, S. F. (2012). Ice-shelf basal channels in a coupled ice/ocean model. *Journal of Glaciology*, *58*(212), 1227–1244.

Gourmelen, N., Goldberg, D. N., Snow, K., Henley, S. F., Bingham, R. G., Kimura, S., ... others (2017). Channelized melting drives thinning under a rapidly melting Antarctic ice shelf. *Geophysical Research Letters*, *44*(19), 9796–9804.

Hamilton, A. K. (2016). *Ice-ocean interactions in Milne Fiord* (PhD thesis). University of British Columbia.

Hamilton, A. K., Laval, B. E., Mueller, D., Vincent, W. F., & Copland, L. (2017). Dynamic response of an Arctic epishelf lake to seasonal and long-term forcing: implications for ice shelf thickness. *The Cryosphere*, *11*(5), 2189–2211.

Hunkins, K. L. (1974). Subsurface eddies in the Arctic Ocean. In *Deep sea research and oceanographic abstracts* (Vol. 21, pp. 1017–1033).

Huttula, T., Pulkkanen, M., Arkhipov, B., Leppäranta, M., Solbakov, V., Shirasawa, K., & Salonen, K. (2010). Modelling circulation in an ice-covered lake. *Estonian Journal of Earth Sciences*, *59*(4), 298.

Inall, M. E., Nilsen, F., Cottier, F. R., & Daae, R. (2015). Shelf/fjord exchange driven by coastal-trapped waves in the arctic. *Journal of Geophysical Research: Oceans*, *120*(12), 8283–8303.

Jackson, J. M., Lique, C., Alkire, M., Steele, M., Lee, C. M., Smethie, W. M., & Schlosser, P. (2014). On the waters upstream of Nares Strait, Arctic Ocean, from 1991 to 2012. *Continental Shelf Research*, *73*, 83–96.

Jackson, P. R., & Rehmann, C. R. (2014). Experiments on differential scalar mixing in turbulence in a sheared, stratified flow. *Journal of Physical Oceanography*, *44*(10), 2661–2680.

Jackson, R. H., Lentz, S. J., & Straneo, F. (2018). The dynamics of shelf forcing in greenlandic fjords. *Journal of Physical Oceanography*, *48*(11), 2799–2827.

Jackson, R. H., Straneo, F., & Sutherland, D. A. (2014). Externally forced fluctuations in ocean temperature at Greenland glaciers in non-summer months. *Nature Geoscience*, *7*(7), 503–508.

Jeffries, M. O. (1985). *Physical, chemical and isotopic investigations of Ward Hunt Ice Shelf and Milne Ice Shelf, Ellesmere Island, NWT* (PhD thesis). University of Calgary.

Jeffries, M. O., Sackinger, W. M., Krouse, H. R., & Serson, H. V. (1988). Water circulation and ice accretion beneath Ward Hunt Ice Shelf (northern Ellesmere Island, Canada), deduced from salinity and isotope analysis of ice cores. *Annals of Glaciology*, *10*, 68–72.

Kindsvater, C. E., & Carter, R. W. (1959). Discharge characteristics of rectangular thin-plate weirs. *Transactions of the American Society of Civil Engineers*, *124*(1), 772–801.

Kirillin, G., Forrest, A., Graves, K., Fischer, A., Engelhardt, C., & Laval, B. (2015). Axisymmetric circulation driven by marginal heating in ice-covered lakes. *Geophysical Research Letters*, *42*(8), 2893–2900.

Kouraev, A. V., Zakharova, E. A., Rémy, F., Kostianoy, A. G., Shimaraev, M. N., Hall, N. M., & Suknev, A. Y. (2016). Giant ice rings on lakes Baikal and Hovsgol: Inventory, associated water structure and potential formation mechanism. *Limnology and Oceanography*, *61*(3), 1001–1014.

Kundu, P., Cohen, I., & Dowling, D. (2012). *Fluid mechanics*. Academic Press, New York, NY.

Laybourn-Parry, J., & Wadham, J. L. (2014). *Antarctic lakes*. Oxford University Press.

Le Brocq, A. M., Ross, N., Griggs, J. A., Bingham, R. G., Corr, H. F., Ferraccioli, F., ... others (2013). Evidence from ice shelves for channelized meltwater flow beneath the Antarctic Ice Sheet. *Nature Geoscience*, *6*(11), 945–948.

Lin, S., Boegman, L., & Rao, Y. (2020). Characterizing spatial and temporal distributions of turbulent mixing and dissipation in lake erie. *Journal of Great Lakes Research*.

McDougall, T. J., & Barker, P. M. (2011). *Getting started with TEOS-10 and the Gibbs seawater (GSW) oceanographic toolbox. SCOR/IAPSO WG127* [type].

Millgate, T., Holland, P. R., Jenkins, A., & Johnson, H. L. (2013). The effect of basal channels on oceanic ice-shelf melting. *Journal of Geophysical Research: Oceans*, *118*(12), 6951–6964.

Mortimer, C. A., Copland, L., & Mueller, D. R. (2012). Volume and area changes of the Milne Ice Shelf, Ellesmere Island, Nunavut, Canada, since 1950. *Journal of Geophysical Research: Earth Surface*, *117*(F4).

Mortimer, C. A., Sharp, M., & Van Wychen, W. (2018). Influence of recent warming and ice dynamics on glacier surface elevations in the Canadian High Arctic, 1995-2014. *Journal of Glaciology*, *64*(245), 450–464.

Mueller, D., Copland, L., & Jeffries, M. O. (2017). Changes in Canadian Arctic ice shelf extent since 1906. In *Arctic ice shelves and ice islands* (pp. 109–148). Springer.

Pedlosky, J. (2013). *Geophysical fluid dynamics*. Springer Science & Business Media.

Pieters, R., & Lawrence, G. A. (2009). Effect of salt exclusion from lake ice on seasonal circulation. *Limnology and Oceanography*, *54*(2), 401–412.

Pnyushkov, A., Polyakov, I. V., Padman, L., & Nguyen, A. T. (2018). Structure and dynamics of mesoscale eddies over the laptev sea continental slope in the arctic ocean. *Ocean Science*, *14*(5).

Rajewicz, J. S. (2017). *Channelized epishelf lake drainage beneath the Milne Ice Shelf, Ellesmere Island, Nunavut* (Unpublished master's thesis). Carleton University.

Rignot, E., & Steffen, K. (2008). Channelized bottom melting and stability of floating ice shelves. *Geophysical Research Letters*, *35*(2).

Rizk, W., Kirillin, G., & Leppäranta, M. (2014). Basin-scale circulation and heat fluxes in ice-covered lakes. *Limnology and Oceanography*, *59*(2), 445–464.

Sciascia, R., Straneo, F., Cenedese, C., & Heimbach, P. (2013). Seasonal variability of submarine melt rate and circulation in an East Greenland fjord. *Journal of Geophysical Research: Oceans*, *118*(5), 2492–2506.

Stanton, T. P., Shaw, W., Truffer, M., Corr, H., Peters, L., Riverman, K., ... Anandakrishnan, S. (2013). Channelized ice melting in the ocean boundary layer beneath Pine Island Glacier, Antarctica. *Science*, *341*(6151), 1236–1239.

Steel, H., McKay, C., & Andersen, D. (2015). Modeling circulation and seasonal fluctuations in perennially ice-covered and ice-walled Lake Untersee, Antarctica. *Limnology and Oceanography*, *60*.

Straneo, F., & Cenedese, C. (2015). The dynamics of Greenland's glacial fjords and their role in climate. *Annual Review of Marine Science*, *7*, 89–112.

Straneo, F., Hamilton, G. S., Sutherland, D. A., Stearns, L. A., Davidson, F., Hammill, M. O., ... Rosing-Asvid, A. (2010). Rapid circulation of warm subtropical waters in a major glacial fjord in East Greenland. *Nature Geoscience*, *3*(3), 182–186.

Timmermans, M.-L., Toole, J., Proshutinsky, A., Krishfield, R., & Plueddemann, A. (2008). Eddies in the Canada Basin, Arctic Ocean, observed from ice-tethered profilers. *Journal of Physical Oceanography*, *38*(1), 133–145.

Turner, J. S. (1968). The influence of molecular diffusivity on turbulent entrainment across a density interface. *Journal of Fluid Mechanics*, *33*(4), 639–656.

Vincent, W., Gibson, J., & Jeffries, M. (2001). Ice-shelf collapse, climate change, and habitat loss in the Canadian high Arctic. *Polar Record*, *37*(201), 133–142.

Washam, P., Nicholls, K. W., Münchow, A., & Padman, L. (2019). Summer surface melt thins Petermann Gletscher Ice Shelf by enhancing channelized basal melt. *Journal of Glaciology*, *65*(252), 662–674.

Williams, W. J., Carmack, E. C., Shimada, K., Melling, H., Aagaard, K., Macdonald, R. W., & Ingram, R. G. (2006). Joint effects of wind and ice motion in forcing upwelling in Mackenzie Trough, Beaufort Sea. *Continental Shelf Research*, *26*(19), 2352–2366.

Zhao, M., Timmermans, M.-L., Cole, S., Krishfield, R., Proshutinsky, A., & Toole, J. (2014). Characterizing the eddy field in the arctic ocean halocline. *Journal of Geophysical Research: Oceans*, *119*(12), 8800–8817.

Figure_1.

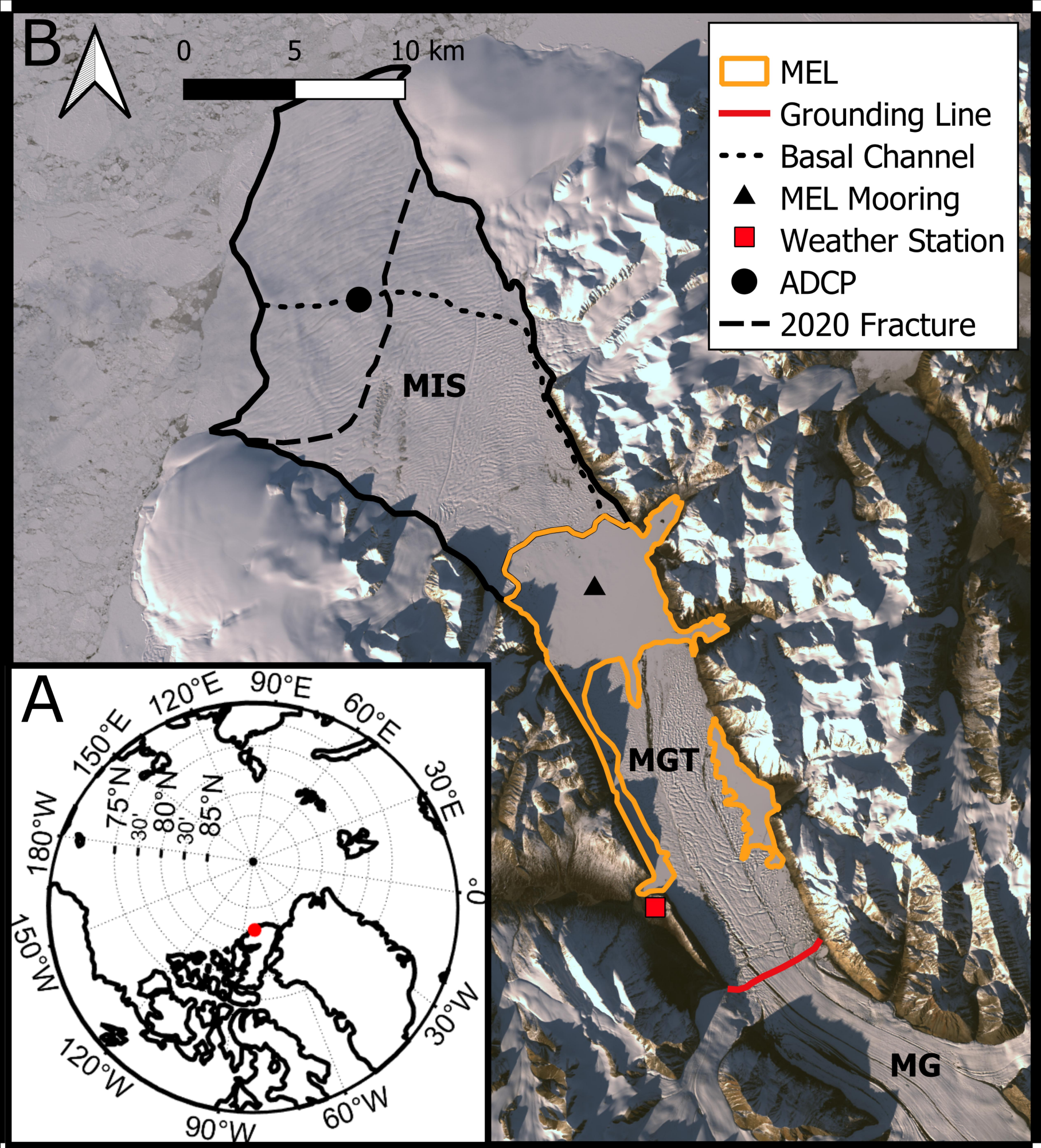
B
0
5
10 km
MEL
Grounding Line
Basal Channel
MEL Mooring
Weather Station
ADCP
2020 Fracture
MIS
MGT
MG
A
120°E
90°E
60°E
150°E
30°E
180°W
0°
150°W
30°W
120°W
60°W
90°W
75°N
80°N
85°N
30'
30'

Figure_2.

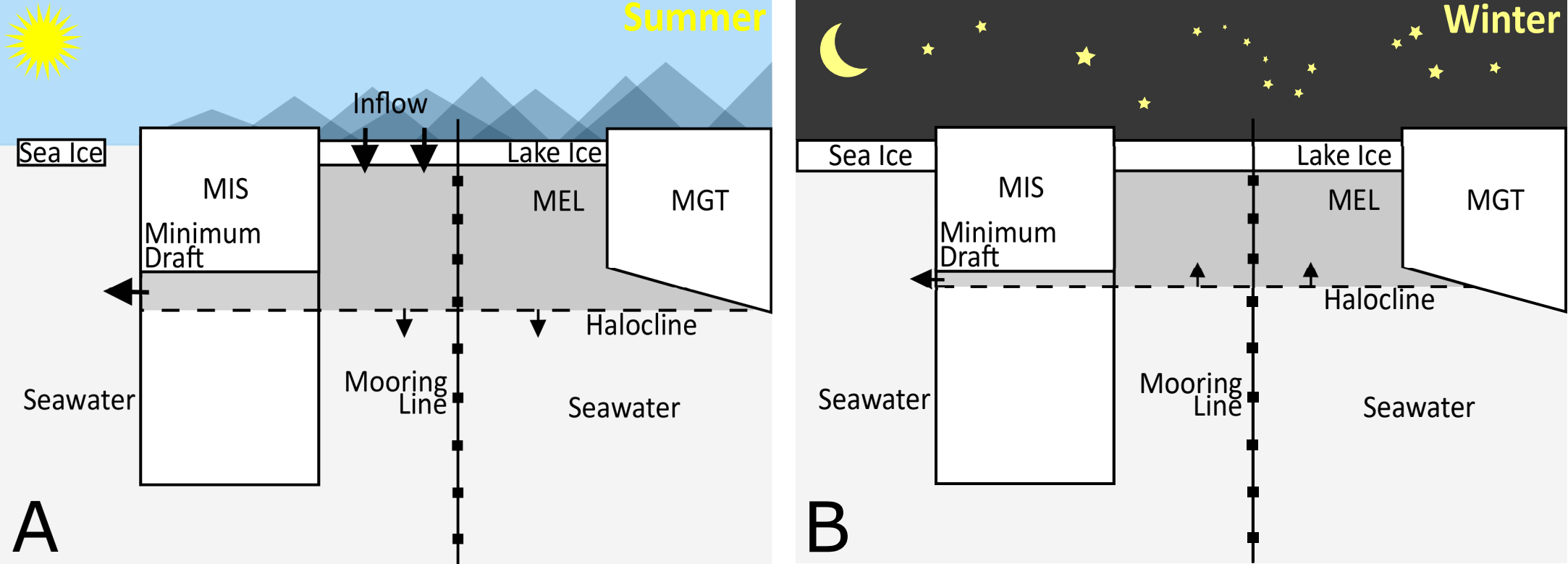
Summer
Inflow
Sea Ice
Lake Ice
MIS
MEL
MGT
Minimum
Draft
Halocline
Seawater
Mooring
Line
Seawater
A
Winter
Sea Ice
Lake Ice
MIS
MEL
MGT
Minimum
Draft
Halocline
Seawater
Mooring
Line
Seawater
B

Figure_3.

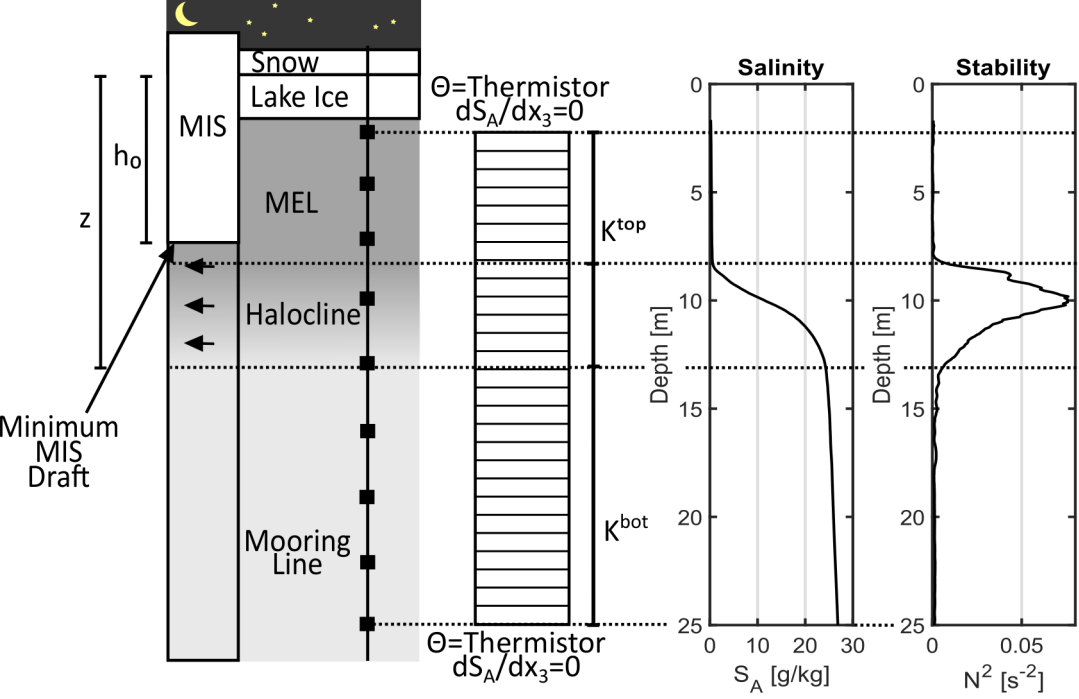
Snow
Lake Ice
MIS
MEL
Halocline
Mooring Line
h_o
z
Minimum MIS Draft
Θ=Thermistor
$dS_A/dx_3=0$
K^{top}
K^{bot}
Θ=Thermistor
$dS_A/dx_3=0$
Salinity
Stability
Depth [m]
0
5
10
15
20
25
0
10
20
30
S_A [g/kg]
0
0.05
N^2 [s^{-2}]

Figure_4.

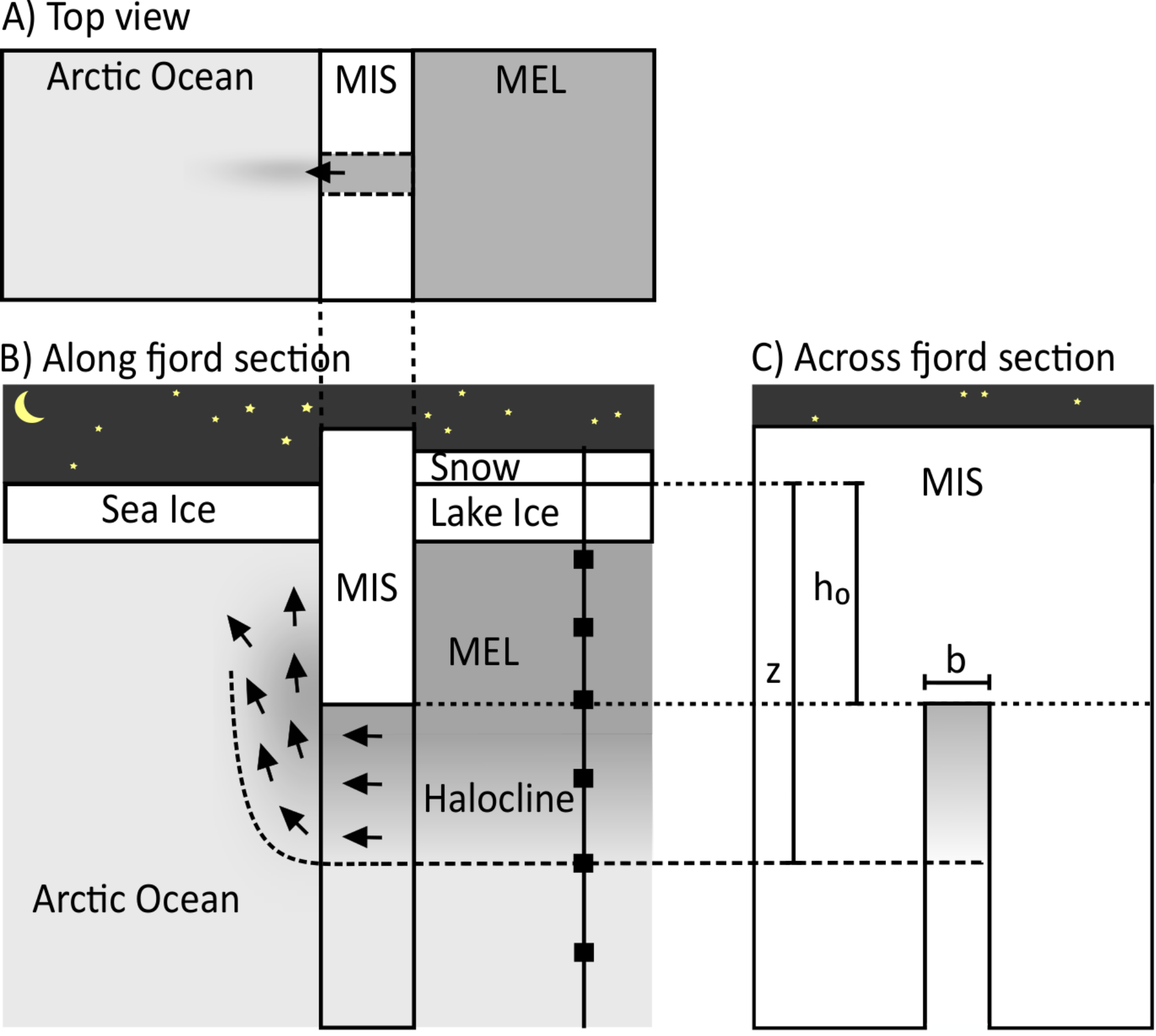
A) Top view
Arctic Ocean
MIS
MEL
B) Along fjord section
C) Across fjord section
Snow
Sea Ice
Lake Ice
MIS
MEL
Halocline
Arctic Ocean
MIS
h_o
z
b

Figure_5.

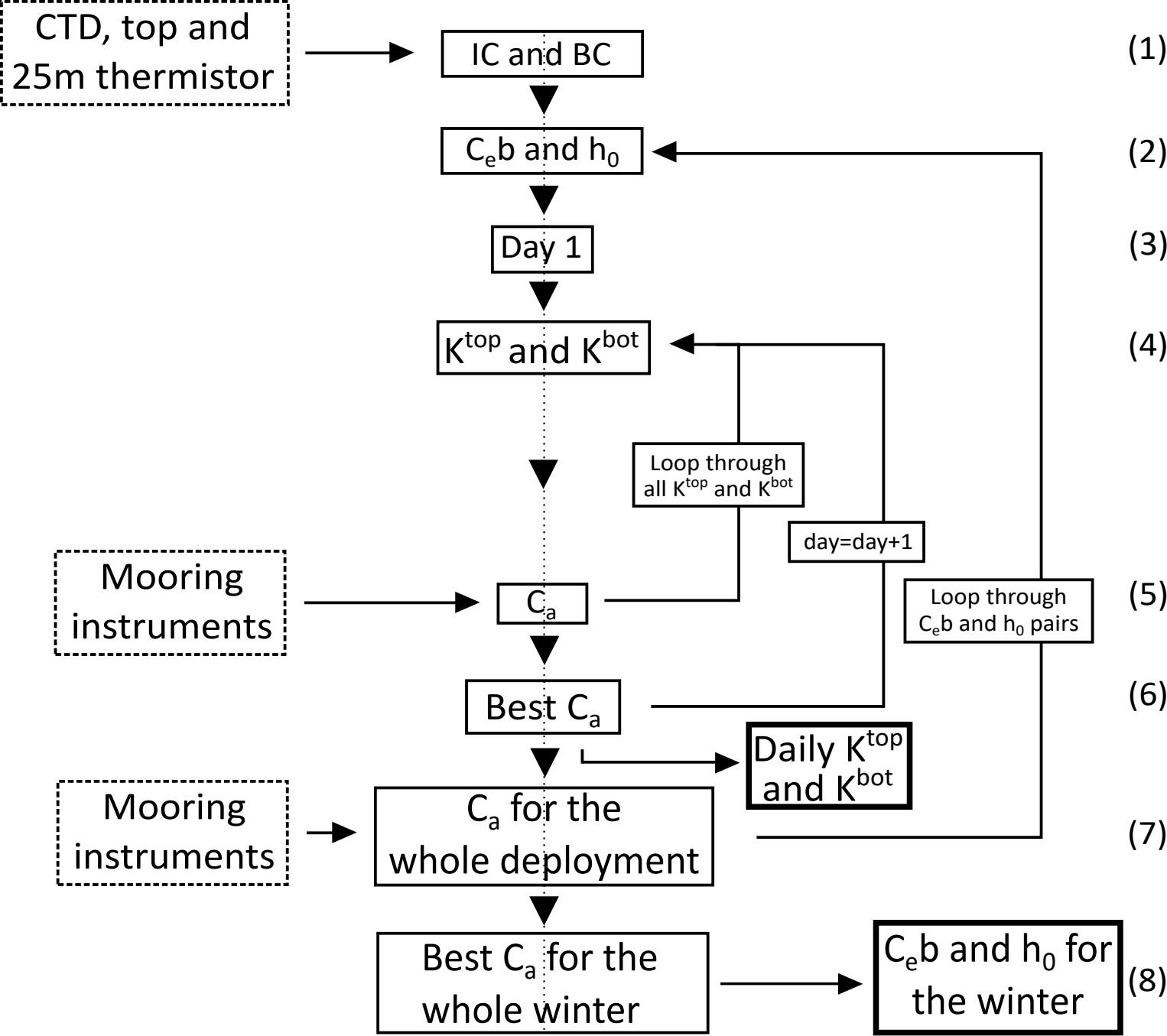
CTD, top and 25m thermistor
IC and BC
(1)
C_eb and h_0
(2)
Day 1
(3)
K^{top} and K^{bot}
(4)
Loop through all K^{top} and K^{bot}
day=day+1
Mooring instruments
C_a
Loop through C_eb and h_0 pairs
(5)
Best C_a
(6)
Daily K^{top} and K^{bot}
Mooring instruments
C_a for the whole deployment
(7)
Best C_a for the whole winter
C_eb and h_0 for the winter
(8)

Figure_6.

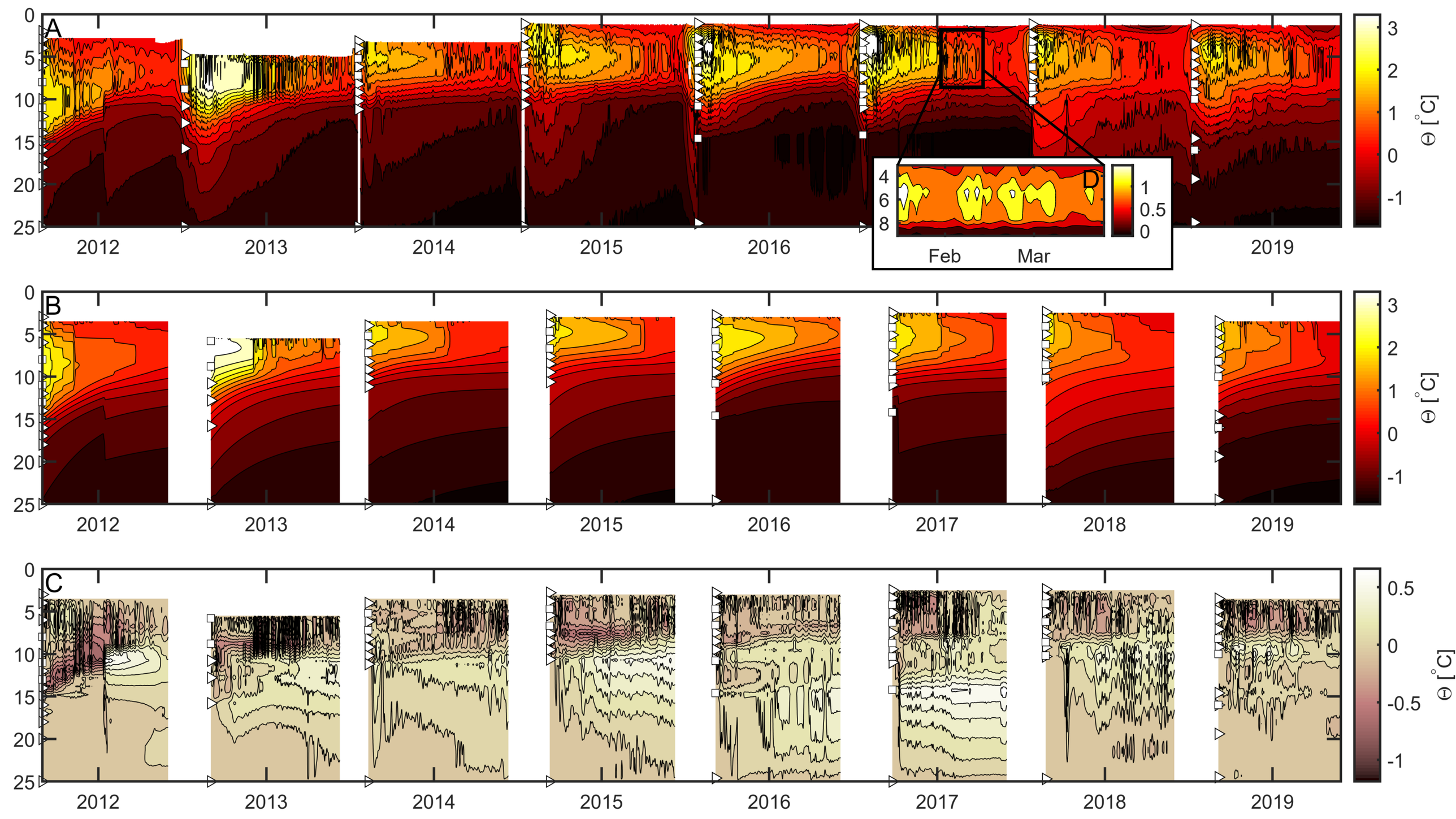
A
B
C
0
5
10
15
20
25
2012
2013
2014
2015
2016
2017
2018
2019
4
6
8
D
1
0.5
0
Feb
Mar
3
2
1
0
-1
Θ [°C]
0.5
0
-0.5
-1

Figure_7.

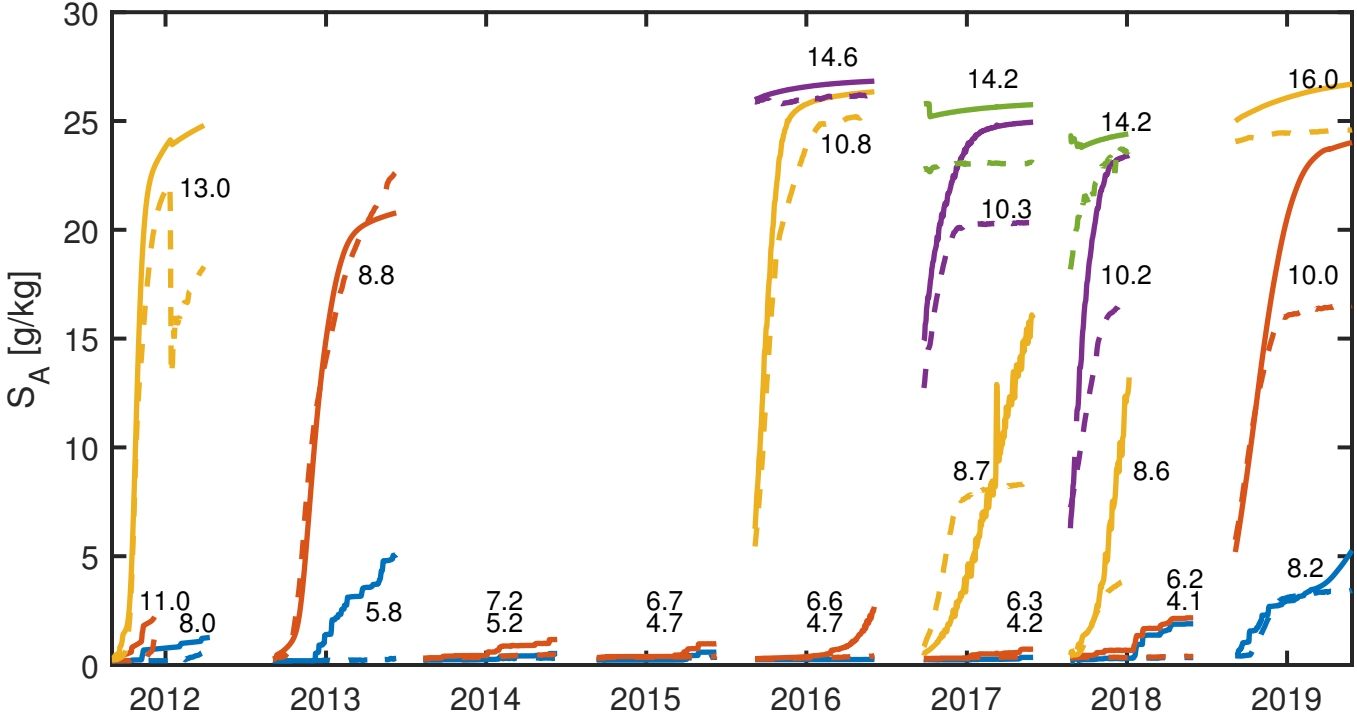
30
25
20
15
10
5
0
S_A [g/kg]
2012
2013
2014
2015
2016
2017
2018
2019
13.0
11.0
8.0
8.8
5.8
7.2
5.2
6.7
4.7
14.6
10.8
6.6
4.7
14.2
10.3
8.7
6.3
4.2
14.2
10.2
8.6
6.2
4.1
16.0
10.0
8.2

Figure_8.

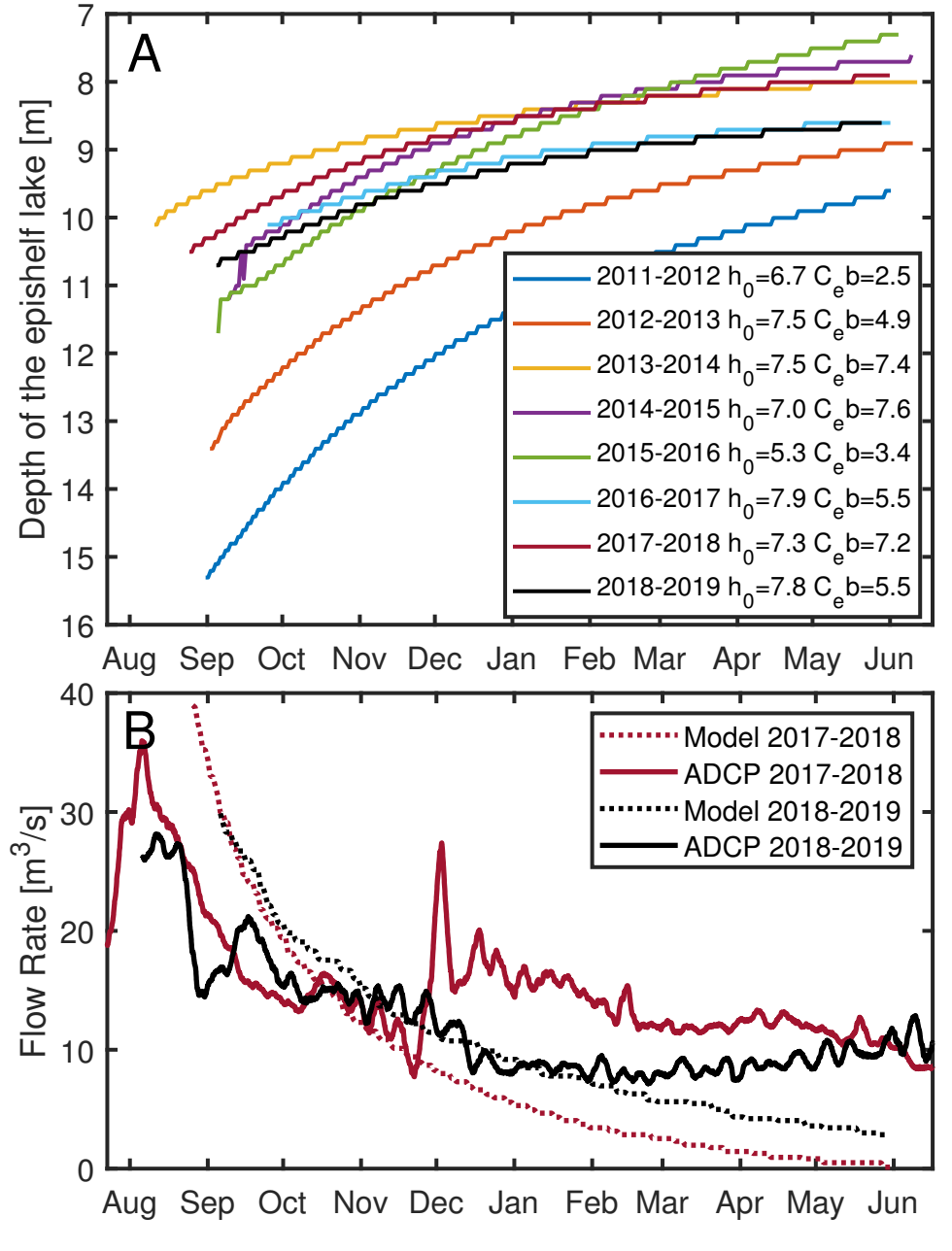
A
Depth of the epishelf lake [m]
7
8
9
10
11
12
13
14
15
16
Aug
Sep
Oct
Nov
Dec
Jan
Feb
Mar
Apr
May
Jun
2011-2012 h0=6.7 Ceb=2.5
2012-2013 h0=7.5 Ceb=4.9
2013-2014 h0=7.5 Ceb=7.4
2014-2015 h0=7.0 Ceb=7.6
2015-2016 h0=5.3 Ceb=3.4
2016-2017 h0=7.9 Ceb=5.5
2017-2018 h0=7.3 Ceb=7.2
2018-2019 h0=7.8 Ceb=5.5
B
Flow Rate [m3/s]
0
10
20
30
40
Model 2017-2018
ADCP 2017-2018
Model 2018-2019
ADCP 2018-2019

Figure_9.

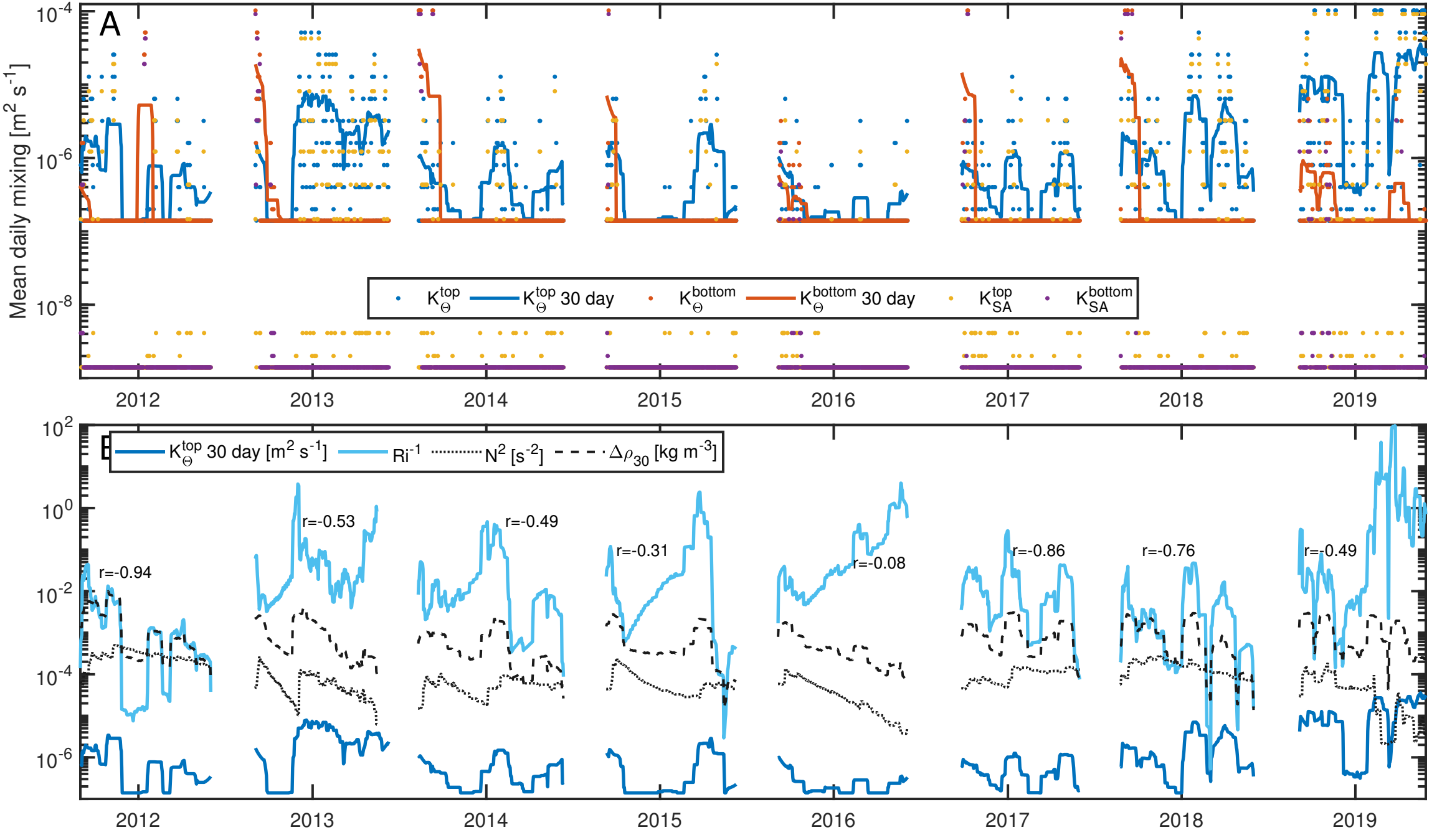
A
Mean daily mixing [m^2 s^{-1}]
10^{-4}
10^{-6}
10^{-8}
K_Θ^{top}
K_Θ^{top} 30 day
K_Θ^{bottom}
K_Θ^{bottom} 30 day
K_{SA}^{top}
K_{SA}^{bottom}
2012
2013
2014
2015
2016
2017
2018
2019
B
K_Θ^{top} 30 day [m^2 s^{-1}]
Ri^{-1}
N^2 [s^{-2}]
$\Delta\rho_{30}$ [kg m^{-3}]
10^{2}
10^{0}
10^{-2}
10^{-4}
10^{-6}
r=-0.94
r=-0.53
r=-0.49
r=-0.31
r=-0.08
r=-0.86
r=-0.76
r=-0.49
2012
2013
2014
2015
2016
2017
2018
2019